



Magnetism of individual atoms adsorbed on surfaces

Harald Brune^{a,*}, Pietro Gambardella^b

^a Institut de Physique des Nanostructures, Ecole Polytechnique Fédérale de Lausanne (EPFL), CH-1015 Lausanne, Switzerland

^b Institut Catalana de Recerca i Estudis Avançats (ICREA) and Centre d'Investigacions en Nanociència i Nanotecnologia (ICN-CSIC), UAB Campus, E-08193 Barcelona, Spain

ARTICLE INFO

Article history:

Available online 10 February 2009

Keywords:

Magnetic impurities
Magnetic anisotropy
Spin–orbit coupling
Dilute magnetic semiconductors
Spin excitation spectroscopy
Spin-polarized transport
Quantized conductance
X-ray circular magnetic dichroism (XMCD)
Scanning tunneling microscopy (STM)

ABSTRACT

Magnetic impurities in solids cause manifold changes in their macroscopic properties, such as anomalous low temperature resistance due to Kondo screening, reduction of the superconducting transition temperature due to local suppression of the order parameter, they create magnetic signatures in semiconductors, and lead to inelastic spin excitations in tunnel junctions. In the present paper we review what has been learnt about these effects from a surface science approach. Placing the magnetic impurities at well defined adsorption sites on single crystal surfaces makes their effect on the host, as well as their own magnetic properties better accessible to experiments, and also better understandable since the atomic environment of the impurity is exactly known lending comparison with theory more direct. After an introduction we discuss X-ray magnetic circular dichroism measurements which are spatially averaging and therefore report on ensemble properties. One of the recent progresses achieved in surface science is the preparation of well defined ensembles, such as surfaces with only single adatoms, each of them in an identical atomic environment and with sufficient mutual distance to exclude interactions. Due to this approach we can now determine the electronic configuration of individual adatoms, their hybridization with the host, and quantify their spin and orbital moments, as well as the spin–orbit induced magneto-crystalline anisotropy, which can be orders of magnitude larger than thin film and bulk values. In the second part we review recent progress in revealing the magnetic properties of individual atoms with the scanning tunneling microscope (STM). With this technique the spatial extent of the Kondo screening cloud and of subgap excitations in the superconductor quasiparticle density of states became apparent. We outline the first pioneering experiments measuring transport through reversible atomic point contacts containing magnetic atoms and measurements using the subgap features caused in superconducting STM tips to detect the magnetism of individual atoms. We then describe experiments using inelastic spin excitation spectroscopy to pin down the magnetic ground state and anisotropy energy of magnetic impurities. We continue with spin-polarized STM experiments reporting magnetization curves of individual magnetic adatoms and finish by a description of the most recent spin-excitation experiments revealing the necessary anisotropy environment for a high spin impurity to display the Kondo effect.

© 2009 Elsevier B.V. All rights reserved.

1. Introduction

The study of magnetic atoms at surfaces is a multifaceted topic that can hardly be classified between the boundaries of a single discipline. The interaction between a magnetic impurity and a non-magnetic metal is a classical condensed matter problem, usually treated in the framework of the Anderson or Kondo models [1]. Owing to their reduced atomic coordination, surface adatoms can further be viewed as a bridge between the atomic and solid state, with many of their electronic and magnetic properties essentially determined by intra-atomic correlation effects [2] that are exem-

plified by the well-known set of rules that go under Hund's name (Fig. 1).

From a surface science perspective, the investigation of the adsorption sites and of diffusion and nucleation processes offers countless opportunities to tune the adatom–substrate interaction, as well as to construct multiatom magnetic clusters of controlled shape, density, and dimensions [3]. Adatoms and clusters may further be considered as the precursors of thin films, as the growth of magnetic mono- and multilayers is typically initiated by the deposition of transition-metal atoms from the vapor phase onto a nonmagnetic substrate. Investigating substrate–impurity hybridization and coordination effects thus provides basic understanding and useful guidelines to tailor the magnetization and magnetic anisotropy of films as well as nanoparticles and to optimize sensitive interface properties that govern the performances of magnetic

* Corresponding author.

E-mail address: Harald.brune@epfl.ch (H. Brune).

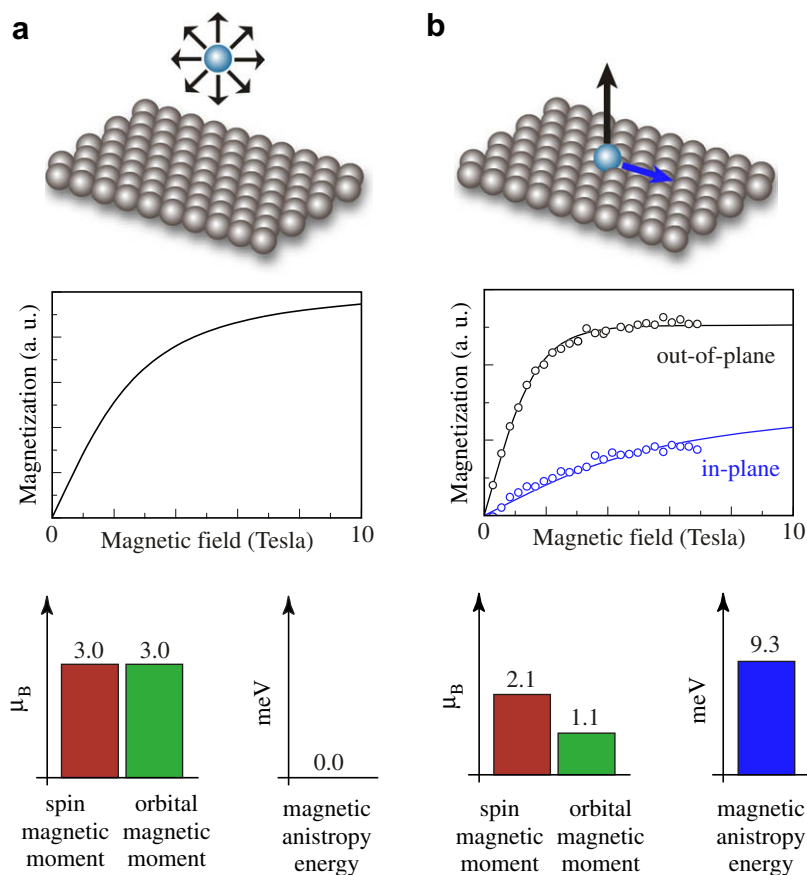


Fig. 1. (a) Spin and orbital magnetic moment of a gas phase Co atom as given by the Hund's rules for a d^7 electronic configuration. (b) Spin and orbital magnetic moment of an individual Co atom deposited on a Pt(111) surface. Both spin and orbital moments are reduced with respect to (a), but remain large compared to bulk Co. The field-dependent magnetization is represented in (a) by a Brillouin function calculated for $T = 5.5$ K. Due to the spherical symmetry of the system the magnetization is isotropic and the magnetic anisotropy energy equals zero. In (b) symmetry breaking and Co–Pt hybridization induce strong anisotropy of the magnetization measured by XMCD along the out-of-plane (black) and close to in-plane direction (blue).

storage media and electron transport in spintronic devices. Finally, adatoms and clusters on nonmagnetic surfaces represent the ultimate paradigm of a nanomagnet, *i.e.*, the smallest entities that can display ferromagnetic behavior.

While the exploitation of such a property for practical applications is presently beyond reach, these systems are attracting increasing attention since they straddle the boundary between classical and quantum magnetism. In a classical picture, the stability of the magnetization orientation of a ferromagnet is determined by the amplitude of the magnetic anisotropy energy barriers, which limit thermally-induced fluctuations of the magnetization and thereby determine the data retention time of a magnetic memory at a given temperature. In quantum systems, such as single-molecule magnets [4], tunneling can cause discrete changes of the spin magnetic quantum number, eventually leading to a finite, temperature-independent probability for magnetization reversal. Surface systems, as will be shown in the following sections, present both classical and quantum behavior, and allow us to explore the transition between these two limits by controlling the adatom–substrate and adatom–adatom interaction. Moreover, and in analogy with single-molecule magnets, one may envisage to test quantum computation [5] and communication schemes [6], with the advantage of working with highly versatile and on the atomic scale well defined structures whose coupling can be adjusted by moving them about on a two-dimensional support.

In this context, the experimental challenge lies in probing extremely small densities of magnetic atoms (typically on the order of 10^{14} atoms/cm² or less) on a macroscopic substrate with nonneg-

ligible para- or diamagnetic response. Until a decade ago, the measurement of surface dilute magnetic impurity systems was restricted to the anomalous Hall effect (AHE) [7,8] and impurity-induced detuning of a thin film superconducting LC oscillator [9]. While these methods provide access to the average impurity magnetization in response to temperature and external magnetic field, techniques based either on X-ray magnetic circular dichroism (XMCD) [10–15] or scanning tunneling microscopy (STM) [16–23] have recently been shown to yield complementary insight into the adatoms electron valence, local spin and orbital moments, magnetic anisotropy, as well as ground and excited magnetic states. STM, moreover, offers the ability to manipulate and address single spins at the atomic scale. The aim of this paper is to review recent progress in this field starting from isolated individual surface atoms and follow the evolution of their magnetic properties as they are incorporated in particles of larger dimensions. The text is organized as follows: Section 2 treats XMCD measurements of individual atoms on nonmagnetic surfaces with strongly different electronic properties, namely an *sp*-metal, K, a transition-metal, Pt, as well as semiconducting Ge and GaAs. Section 3 introduces to most recent progress achieved in characterizing individual magnetic atoms by means of STM.

2. Magnetism of individual surface atoms probed by XMCD

X-ray absorption spectroscopy (XAS) applied to the study of magnetic materials has found widespread application thanks to the advent of intense sources of circularly polarized light with tun-

able energy, soft X-ray monochromators, and dedicated experimental endstations [24]. Because X-ray transitions are localized on atoms and polarization dependent, XAS probes the valence shell occupation number as well as the symmetry of the unoccupied electron orbitals; in other words, the lineshape and relative strength of the XAS features are a fingerprint of the chemical state of a given atom. As the X-ray absorption intensity for circularly polarized light depends on the orientation of the spin and orbital moment of the unoccupied electron states relative to the X-ray helicity, magnetic sensitivity is achieved by taking the difference of absorption spectra for parallel (I^+) and antiparallel (I^-) alignment of the X-ray helicity with respect to the sample magnetization. XMCD spectra obtained in this way allow one to identify the magnetization direction and strength of a given element, and to estimate quantitatively the spin (m_s) and orbital (m_L) magnetic moments by means of the so-called XMCD sum rules [25–27]. Due to the limited escape depth of low-energy photoelectrons, XAS measured in the total electron yield mode [24] is inherently surface sensitive, and has been shown to probe dilute surface impurities with a concentration down to 3×10^{12} atoms cm^{-2} , corresponding to about 0.002 monolayers (ML) [10].

The XMCD experiments reported here were performed on beamline ID08 of the European Synchrotron Radiation Facility located in Grenoble, using the photon beam provided by an APPLE II undulator source with $99 \pm 1\%$ circular polarization rate and energy resolution set to about 200 meV. The sample, tightly screwed at the bottom of a liquid helium flow cryostat, was placed in a thermally-shielded environment between the two coils of a superconducting split magnet, which produced a variable field \mathbf{B} of up to 7 T collinear with the incident X-ray direction. To probe both the out-of-plane and in-plane magnetic moments the sample was rotated with respect to \mathbf{B} and the X-ray beam by an angle θ comprised between 0° (normal incidence) and 70° (grazing incidence). XAS measurements were performed by recording the sample drain current as a function of X-ray energy normalized to the incoming photon

flux given by the photocurrent of a gold grid reference monitor. Measurements were taken over the $L_{2,3}$ absorption edges of Mn, Fe, Co, and Ni, corresponding to the excitation of $2p$ core electrons into empty $3d_{4s}$ states.

2.1. 3d impurities on *sp*-metal substrates

The behavior of transition-metal impurities in nonmagnetic metal hosts has attracted attention ever since the discovery of the Kondo resistance minimum [28]. It is widely recognized that the extent to which the transition-metal d -states mix with the valence bands of the host directly influences macroscopic measurable properties such as the electric conductivity, magnetic susceptibility, and specific heat. The work of Friedel [29] and Anderson [30] on the interaction of a single localized non-degenerate d orbital with a free-electron gas constitutes the basis of our current understanding of such systems. As shown by Anderson, the preservation of the impurity magnetic moment depends on the balance between the Coulomb repulsion between electrons with opposite spins, the hybridization energy between the localized orbital and the conduction band states of the metal, and the host electron density. As it turns out, these factors influence not only the existence of a magnetic moment, but also its description in terms of quantum or classical operators. To address such issues in a surface context, a series of experiments was performed on alkali metal substrates, which, owing to their simple *sp* electronic structure represent ideal hosts for studying the interaction between localized $3d$ states and a free-electron Fermi sea.

The electronic ground state of Fe, Co, and Ni impurities in alkali metal hosts has been debated among experimentalists [31–38] and theorists [39,40] for over a decade, in particular with respect to the $3d$ -valence state, the local moment at the impurity sites, and the orbital contribution to the total magnetic moment. By combining XAS and XMCD the ground state and the magnetic moments of Fe, Co, and Ni impurities on alkali metal surfaces could directly

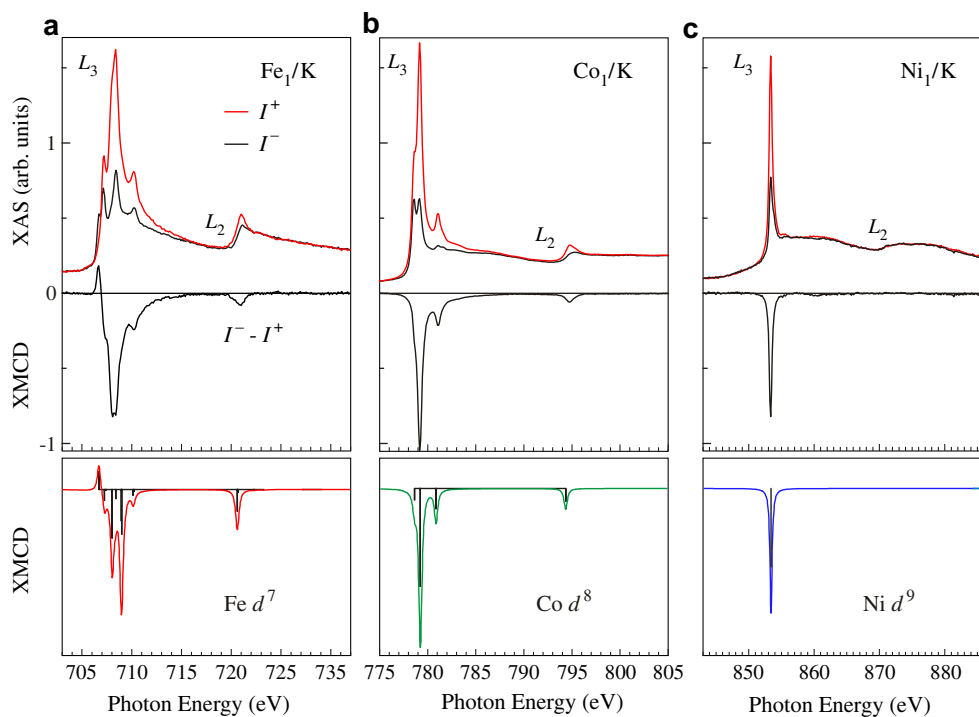


Fig. 2. XAS spectra recorded over the $L_{2,3}$ edges with parallel (I^+ , red line) and antiparallel (I^- , black line) alignment of the photon helicity to the impurity magnetic moment for (a) 0.015 ML Fe, (b) 0.015 ML Co, and (c) 0.004 ML Ni deposited on K films. The XMCD is shown as $I^- - I^+$ consistent with the scale of the XAS units. The bottom panels show the calculated XMCD spectra for d^7 , d^8 , and d^9 atomic configurations. Adapted from [10].

be determined [10]. Fig. 2 shows the XAS spectra of Fe, Co, and Ni individual impurities on K films. The impurities were quench-condensed at $T = 10$ K on multilayer K films previously prepared on a Cu(111) surface. The difference with the corresponding bulk elemental spectra [24] is striking: the impurities XAS present narrow multiplet structures instead of two broad absorption resonances at the L_3 and L_2 edges, indicating strong localization of the $3d$ electrons at the impurity site. Even more remarkably, the comparison of the experimental data with atomic multiplet calculations [41] for $2p^63d^n \rightarrow 2p^53d^{n+1}$ transitions (see bottom panels of Fig. 2) indicates that Fe, Co, and Ni have atomic-like ground states with predominant d^7 , d^8 , and d^9 character, respectively. Thus, hybridization between d and sp states is, in this case, very limited; the influence of crystal field interactions is also small, likely due to the high delocalization of the conduction band states of the substrate. On the other hand, the magnitude of the XMCD is significantly larger compared to transition-metal bulk atoms and metallic nanostructures [27,42], and consistent with the expectation values of full Hund's rules magnetic moments at finite temperature and magnetic field, as reported in Table 1. In particular, the negative (vanishing) XMCD intensity at the L_2 edge for Fe and Co (Ni) is an uncommon signature of the unquenched orbital moment typical of strongly correlated electrons in free atoms. The expectation values of m_L , m_S , and the spin dipole moment (m_T) projected along the X-ray beam direction are related by the sum rules [25,26] to the integrated XMCD signal. Here we report the ratio, $R = m_L/(m_S + m_T)$, which can be calculated self-consistently from the XMCD spectrum alone (i.e., without normalization to the isotropic XAS intensity)

Table 1

Calculated Hund's rules ground state values of the isotropic spin magnetic moment (m_S) and dipole spin magnetic moment (m_T), orbital magnetic moment (m_L), total angular momentum (J) and magnetic moment $m = g_J \mu_B \sqrt{J(J+1)}$, where g_J is the Landé g -factor, corresponding to the $3d$ configurations identified on K films. The atomic and experimental R values are also compared for 0.015 ML Fe, 0.015 ML Co and 0.004 ML Ni.

	m_S	m_T	m_L	J	m	R_{at}	R_{exp}
Fe d^7	3	-1	3	9/2	$6.63 \mu_B$	3/2	0.95 ± 0.05
Co d^8	2	1	3	4	$5.59 \mu_B$	1	0.89 ± 0.04
Ni d^9	1	2	2	5/2	$3.55 \mu_B$	2/3	0.67 ± 0.05

[27] and which is temperature and field independent in as much these parameters do not affect the mixing of electron states with different total angular momentum J . We find a very good agreement between R_{exp} deduced from the XMCD measurements and R_{at} calculated in the atomic limit for Co and Ni. For Fe there is a discrepancy which is due partly to the imperfect matching of the measured and calculated d^7 XMCD, but that persists also for $R = 1.25$ extracted from the theoretical d^7 spectrum in Fig. 2a and is possibly related to finite temperature effects. We note that the mismatch between the Fe/K and calculated d^7 XMCD may be reduced by fine tuning the Slater integral parameters, which has not been done here in order to present the same type of calculation for Fe, Co, and Ni.

These measurements allowed us to resolve the ground state and magnetic moment of $3d$ impurities on an alkali metal [33–40], as well as to test the validity of the XMCD sum rules in the precise context of their derivation, i.e., that of a localized atomic model [25,26] where m_T is not negligible as commonly assumed in itinerant metals [27]. Moreover, there is another important aspect that stands out, namely the fact that $3d$ atoms deposited on a metal surface may preserve their atomic-like properties, in particular the quantization of the spin and orbital moments. This is at variance with the observation of classically behaving Co impurity magnetization on transition-metal substrates, as shown later in Section 2.2. In the case of the alkali metals, we find that transition-metal atoms placed in contact with a low-density free-electron gas (as is the case for a K surface) undergo an $s \rightarrow d$ charge transfer of +1 electron, while the atomic character of the d -states remains almost unperturbed (see also Fig. 3c). This is not easily explained in the case of the Anderson model, where intra-atomic and s - d interactions are treated on equal footing [30]. Rather, our observations call for considering the atomic many-electron states as zero-order terms of a model Hamiltonian in which interactions with the conduction electrons are treated perturbatively. This approach was explored by Hirst in the 1970s [43], but given only limited recognition for the lack of direct supporting evidence. However, it leads naturally to d -shell configurations with integer occupation numbers, determined by the balance between impurity attractive potential and repulsive local Coulomb interactions, and to atomic-like m_S and m_L values. In this model, the correlation effects rep-

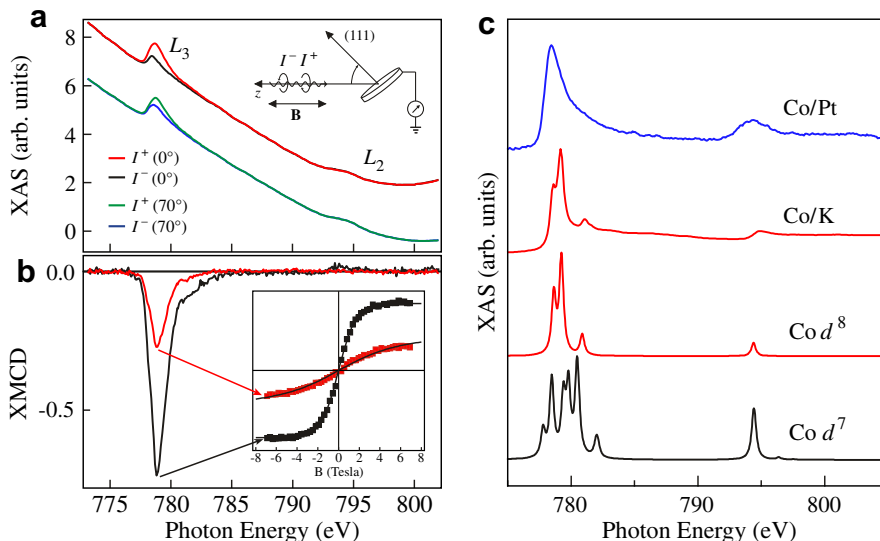


Fig. 3. (a) $L_{2,3}$ XAS spectra of Co impurities (0.03 ML) deposited on Pt(111) and recorded at $T = 5.5$ K, $B = 7$ T with parallel (I^+) and antiparallel (I^-) alignment of the photon helicity with respect to \mathbf{B} at an angle $\Theta = 0^\circ$ relative to the surface normal. (b) XMCD ($I^- - I^+$) for $\Theta = 0^\circ$ and 70° at $B = 7$ T. Inset: field-dependence of L_3 -XMCD for both field directions. Adapted from [11]. (c) Comparison between the total XAS ($I^+ + I^-$) after background subtraction for Co impurities on Pt(111), Co impurities on a K film, and the calculated XAS for atomic-like d^8 and d^7 configurations.

resented by the Hund's rules can only be broken at a large cost of energy, corresponding to the gap between different d^n atomic configurations, which becomes possible only in the limit of very large host conduction electron density. If such a gap can be overcome, the impurity d electrons merge into broadened virtual bound states by mixing with the host s states, as in the Friedel-Anderson approach. This is indeed observed for $3d$ impurities deposited on Na, Li, and Cu surfaces, where the free-electron density is roughly a factor 2, 3, and 6 larger compared to K, respectively. The surface electron density therefore turns out to be the crucial parameter determining the extent to which the impurity d -states mix with the host conduction electrons and thereby governing the magnitude and quantization of the adatom magnetic moment.

2.2. Co impurities on Pt(111)

Transition-metal substrates differ from alkali metals not only due to their much larger conduction electron density, but also for the presence of unfilled d -states crossing the Fermi level, which heavily affect most of their magnetic properties (e.g., the susceptibility and magnetoresistance) as well as the nonmagnetic ones (e.g., cohesion, diffusion barriers, catalytic activity, etc.). As an example of a strongly interacting substrate we present the data for isolated Co impurities on Pt(111). The adatom XAS spectra in Fig. 3a show relatively weak absorption features compared to the Pt background due to the extremely low concentration of Co adatoms and intense Pt absorption. However, the substrate background can be measured before the adatom deposition and subsequently subtracted, as done for the experimental XAS (I^+ + I^-) spectra shown in Fig. 3c, and it cancels out automatically in the XMCD. The top spectrum of Fig. 3c shows the XAS of Co/Pt(111) and reveals broad features typical of Co metal that are drastically different from the XAS calculated for the vapor-phase d^7 Co configuration shown in the lower spectrum. The spectrum of Co/Pt(111) differs also from that of Co impurities deposited on free-electron metals, where, as we have seen in Section 2.1, the narrow XAS multiplet structure indicates that the Co ground state has d^8 atomic-like character. On Pt, the impurity $3d$ -states hybridize strongly with both the $5d$ and $6s$ -states of the substrate. Electron delocalization leads to a reduction of intra-atomic correlation effects, causing a substantial decrease of m_S and m_L compared to the vapor-phase. As shown in the diagram of Fig. 1, the impurity magnetic moments are nonetheless significantly larger than the ones in bulk Co, where $m_S = 1.52$ and $m_L = 0.15 \mu_B$. According to the XMCD sum rules, the vanishing intensity of the XMCD at the L_2 edge in Fig. 3b indicates that m_L is unusually large for a transition-metal system, with a saturation value $m_L = 1.1 \pm 0.1 \mu_B$ measured at $T = 5.5$ K and $\mathbf{B} = 7$ T applied out-of-plane. This value represents a strong enhancement even with respect to 2D films [44–46], supported nanoparticles [46,47], and 1D atomic chains [42,12]. As shown also by ab-initio calculations [11,48–50], this trend is naturally to be attributed to the reduced coordination of the impurities, establishing a gradual transition from the atomic to the bulk limit governed by the substrate–adatom and lateral adatom–adatom interactions.

Given the pronounced anisotropic spatial extension of the d -orbitals, the Co–Pt admixture of $3d$ and $5d$ states may lead to unequal filling of wavefunctions with different symmetry, and hence to a strong anisotropy of the orbital magnetization. As the spin–orbit coupling between m_S and m_L is taken into account, a strong magnetic anisotropy of the overall magnetization is to be expected. Indeed, the magnitude of the XMCD relative to the XAS intensity measured for $\mathbf{B} = 7$ T applied out-of-plane ($\theta = 0^\circ$) and close to in-plane ($\theta = 70^\circ$) differs by more than 60%, revealing the presence of extraordinary magnetic anisotropy for the Co adatoms in contact with the Pt(111) surface. The magneto-crystalline anisotropy en-

ergy can be determined by means of XMCD by measuring the field dependence of the L_3 minimum along different directions with respect to the substrate normal, as shown in the inset of Fig. 3b. The fixed-energy L_3 intensity depends on the linear combination $m_S + 3m_L + m_T$ [25,26], but it can be demonstrated that the three moments m_S , m_L , and m_T follow the same field dependence, i.e., that the XMCD L_3 signal is proportional to the total Co magnetic moment. We find that the adatom magnetization can be adequately fitted in the framework of a classical model, where the time-averaged projection of the total impurity moment (m) on the magnetic field direction is given by

$$\langle m \rangle = m_0 \frac{\int \hat{\mathbf{m}} \cdot \hat{\mathbf{B}} \exp[(\mathbf{m} \cdot \mathbf{B} + K(\hat{\mathbf{m}} \cdot \hat{\mathbf{e}})^2)/k_B T] d\Omega}{\int \exp[(\mathbf{m} \cdot \mathbf{B} + K(\hat{\mathbf{m}} \cdot \hat{\mathbf{e}})^2)/k_B T] d\Omega} \quad (1)$$

Here, m_0 stands for the saturation value of the Co plus induced Pt moment, $\hat{\mathbf{e}}$, $\hat{\mathbf{m}}$, and $\hat{\mathbf{B}}$ represent the unit vectors of the easy axis, the magnetic moment, and the field direction, respectively, K is a uniaxial magnetic anisotropy barrier, and the integration is carried out over the solid angle Ω of the magnetic moment in spherical coordinates. The solid lines represent fits of the data by means of numerical integration of Eq. (1) with m and K as free parameters fitted simultaneously for the two curves. Note that, in such a model, all directions are in principle allowed for the Co magnetic moment, showing that a classical description is well-suited to describe a strongly hybridized impurity system, contrary to the case discussed in Section 2.1. Moreover, owing to the strong Stoner enhancement factor of Pt, the substrate atoms are highly polarized by $3d$ transition-metal species, developing a significant intrinsic magnetization that decays exponentially away from the impurity site. In dilute bulk CoPt alloys with 1% at. Co concentration, the total moment per Co atom is of the order of $10 \mu_B$ [51]. In our case of surface dilute impurities, the fit of Eq. (1) yields $m = 5.0 \pm 0.6 \mu_B$ and $K = 9.3 \pm 1.6$ meV. These values remain unchanged on samples with Co coverage comprised between 0.007 and 0.03 ML showing that magnetic or electronic interactions between the adatoms are negligible.

The magnetic anisotropy energy of individual Co adatoms is remarkably large even compared to typical hard magnetic systems such as SmCo_5 ($K = 1.8$ meV per Co atom [52]), Co/Pt and Co/Au multilayers ($K = 0.3$ meV per Co atom [53,52]). Different effects combine in building up such giant anisotropy energy barriers for Co atoms on Pt(111): (i) the broken symmetry of the adatoms as compared to the vapor phase constitutes the necessary condition to exhibit anisotropic behavior. (ii) The reduced coordination leads to $3d$ -electron localization, which augments the orbital and spin magnetic moments as well as the spin–orbit energy due to increases in the local density of states near the Fermi level [54,55]. (iii) The strong spin–orbit coupling of the Pt $5d$ -states results in additional magnetic anisotropy energy of the induced magnetization [11], an effect common to all CoPt compounds [56]. While (i) determines the angular dependence of the magnetic anisotropy energy, (ii) and (iii) determine its magnitude. Indeed, the Co/Pt combination was chosen in order to maximize magnetic anisotropy effects, since hcp-Co presents the largest anisotropy among $3d$ ferromagnetic elements ($K = 0.45 \times 10^7$ erg/cm³ = 0.045 meV/atom compared to, e.g., 0.005 meV/atom for Fe [57]) and L1₀-ordered Co₅₀Pt₅₀ alloys have $K = 0.8$ meV/Co atom [52].

It is well-known that size effects in metallic nanoparticles with a high ratio of surface to volume atoms influence the saturation magnetization in cluster beams [58] as well as in surface-supported systems [46,59,47,60,61]. Such effects become dominant as we reach close to single-digit nanometer dimensions. In this critical size regime, key questions are how the magnetic anisotropy energy evolves from single atoms to finite-sized particles, how it correlates to the atomic magnetic moments, and how both depend on the details of the atomic coordination.

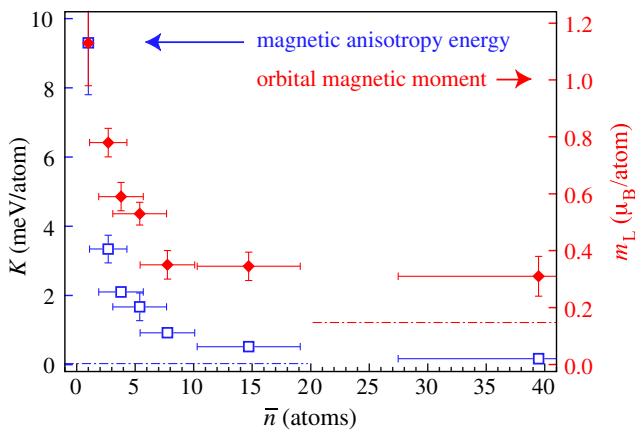


Fig. 4. (a) Orbital moment m_L and anisotropy energy K as a function of the average island size \bar{n} for Co/Pt(111). For comparison, the red and blue dashed-dotted lines show the MAE per Co atom of the L_{10} CoPt alloy and hcp-Co, respectively. The error bars on the horizontal scale represent the standard deviation of the size distribution determined by STM. Adapted from [11].

By using the energetic hierarchy of surface diffusion processes [3], we have studied the development of the magnetic moments and magnetic anisotropy in monolayer high Co particles starting from isolated adatoms to 2D islands with an average size of $\bar{n} = 40$ atoms. While m_s is expected to vary in a fairly restricted range between 2.1–2.2 μ_B for an individual impurity [11,49] and 1.8–1.9 μ_B for a continuous 2D layer [62], as the majority spin band is almost filled in all such cases, m_L is much more sensitive to changes in the atomic coordination, reflecting its closer link with the symmetry and relative filling of the d -orbitals. Fig. 4 shows the progressive quenching of m_L as a function of average particle size \bar{n} . Remarkably, the largest changes of m_L are observed for the smallest particles: for $\bar{n} = 3$ and 4 atoms m_L has already reduced to 0.78 and 0.59 μ_B , respectively. The magnetic anisotropy energy, as expected, is strongly correlated to the decrease of m_L showing similar drastic changes for one-atom variations of the atomic coordination. For $\bar{n} = 3$ atoms, $K = 3.3$ meV amounts to only 30% of the individual impurity value, while K drops below the anisotropy energy of the equi-atomic CoPt alloy already for $\bar{n} > 10$.

The trend evidenced in Fig. 4 shows that an increase by one to two orders of magnitude in magnetic anisotropy energy with respect to bulk or 2D films can be obtained by reducing the size of magnetic particles to a few tens of atoms or less on suitable substrates. While this holds on a per atom basis, it is obvious that the overall stability of the particle magnetization is governed by the sum of the atomic anisotropy energy contributions. As more atoms are assembled together to fabricate particles with a large total magnetic moment and a total K strong enough to stabilize ferromagnetic behavior against thermal fluctuations, this gain is countered by the decrease of K per atom with increasing \bar{n} . The problem, however, can be circumvented by noting that the atomic coordination rather than the absolute particle size is the key parameter that governs the magnitude of K , m_L , and m_s . Surface supported nanostructures where the shape and composition are tuned so as to control the coordination of the magnetic atoms and maximize useful interface effects, such as in core-shell particles [63] and nanowires [64,65], offer very interesting opportunities to exploit such effects.

2.3. Mn impurities on Ge and GaAs surfaces

The investigation of 3d impurities diluted in semiconducting hosts has attracted enormous interest in recent years thanks to the discovery of ferromagnetism in $(\text{Ga}_{1-x}\text{Mn}_x)\text{As}$ [66] and

$\text{Mn}_x\text{Ge}_{1-x}$ [67] epitaxial films. Interesting questions in this field relate to the magnetic properties of Mn adsorbed on Ge and GaAs substrates, in particular to the magnitude of the local magnetic moment of Mn in a semiconducting matrix and the possibility to induce two-dimensional ferromagnetism in a Mn-doped surface δ -layer. Efforts aimed at understanding and optimizing the mechanisms responsible for Mn-induced magnetic order in bulk-like films face the problem that the growth conditions [68] and post-growth annealing procedures [69–71] affect the Curie temperature and the saturation magnetization in a way that is often hard to control, as the concentration and distribution of Mn dopants, the charge carrier density, the presence of structural defects such as Mn interstitials, Mn clusters, and As antisites in $(\text{Ga}_{1-x}\text{Mn}_x)\text{As}$ significantly influence the magnitude and sign of the magnetic coupling. A well-known example of this situation is the magnetization deficit that is found both in $(\text{Ga}_{1-x}\text{Mn}_x)\text{As}$ [72–76] and $\text{Mn}_x\text{Ge}_{1-x}$ [67] when comparing the experimental saturation magnetization with that predicted on the basis of the Mn concentration and theoretical estimates of the Mn local moment. Deviations from the expected 4 μ_B [77,78] and 3 μ_B [67,79,80] per Mn atom in $(\text{Ga}_{1-x}\text{Mn}_x)\text{As}$ and $\text{Mn}_x\text{Ge}_{1-x}$ are in the range of 20–80% [72,73] and 45–60%, respectively. The study of surface impurities, on the other hand, reveals Mn moments in agreement with theoretical estimates and has allowed to identify the origin of the magnetization deficit [13].

For these studies, single crystal Ge(100), Ge(111), and GaAs(110) surfaces were prepared in ultra-high-vacuum by repeated Ar^+ sputtering and annealing cycles to 650 °C. The clean Ge(100) and Ge(111) surfaces showed the characteristic low-energy electron diffraction (LEED) patterns of the (2×1) and $c(2 \times 8)$ reconstructions, respectively, and GaAs(110) the expected (1×1) LEED pattern, although the precise stoichiometry of this surface remained undetermined, as preferential sputtering of As is likely to lead to Ga-rich surface layers. Mn atoms were deposited at a temperature of 5 K to inhibit surface diffusion and subsequent cluster formation and with coverages below the nucleation threshold of statistical growth defined by the coverage where 10% of the islands are dimers and situated for square lattices at 0.05 ML [3]. Coverages of up to 0.35 ML were investigated, where 1 ML = 6.2×10^{14} atoms/cm² for the bulk-truncated Ge(100) surface is taken as a reference unit. Fig. 5a shows the circularly polarized XAS spectra for individual Mn atoms deposited on Ge(100), Ge(111), and GaAs(110) recorded at 5 K with applied field $\mathbf{B} = 6$ T. As for Co/Pt, the impurity $L_{2,3}$ XAS is superposed to a strong nonmagnetic background signal from the substrate, which gives no contribution to the XMCD, shown in (b). XAS and XMCD spectra are also reported for individual Mn atoms deposited on a K film and for a d^5 ground state calculated within a multiplet approach [41]. Contrary to Fe, Co, and Ni impurities investigated in the previous section, which change their atomic ground state from d^n to d^{n+1} , Mn is found to retain a pure d^5 configuration on K owing to the stability of a half-filled d -shell. It is therefore practical to adopt Mn/K spectra as representative of a pure $^6S_{5/2}$ ground state, justified also by the excellent agreement with the calculated Γ^+ , Γ^- , and $\Gamma^- - \Gamma^+$ spectra for such a configuration and the Brillouin fit of the XMCD magnetization with $J = 5/2$ reported in Fig. 5c.

Mn/Ge(100), Ge(111), and GaAs(100) XAS and XMCD spectra present broader multiplet features compared to Mn/K, revealing that the ground state of Mn atoms in contact with Ge and GaAs surfaces is not purely d^5 owing to varying degrees of hybridization of the impurity d -states on different substrates, similarly to what is observed for submonolayer Mn films on metal surfaces [81]. This result is in contrast with previous XMCD studies of $(\text{Ga}_{1-x}\text{Mn}_x)\text{As}$, where the XAS was interpreted in terms of either pure d^5 [73] or a $d^4 - d^5 - d^6$ [76,82] admixture, but the XMCD was invariably assigned to the pure d^5 state with the hypothesis of coexisting magnetic and

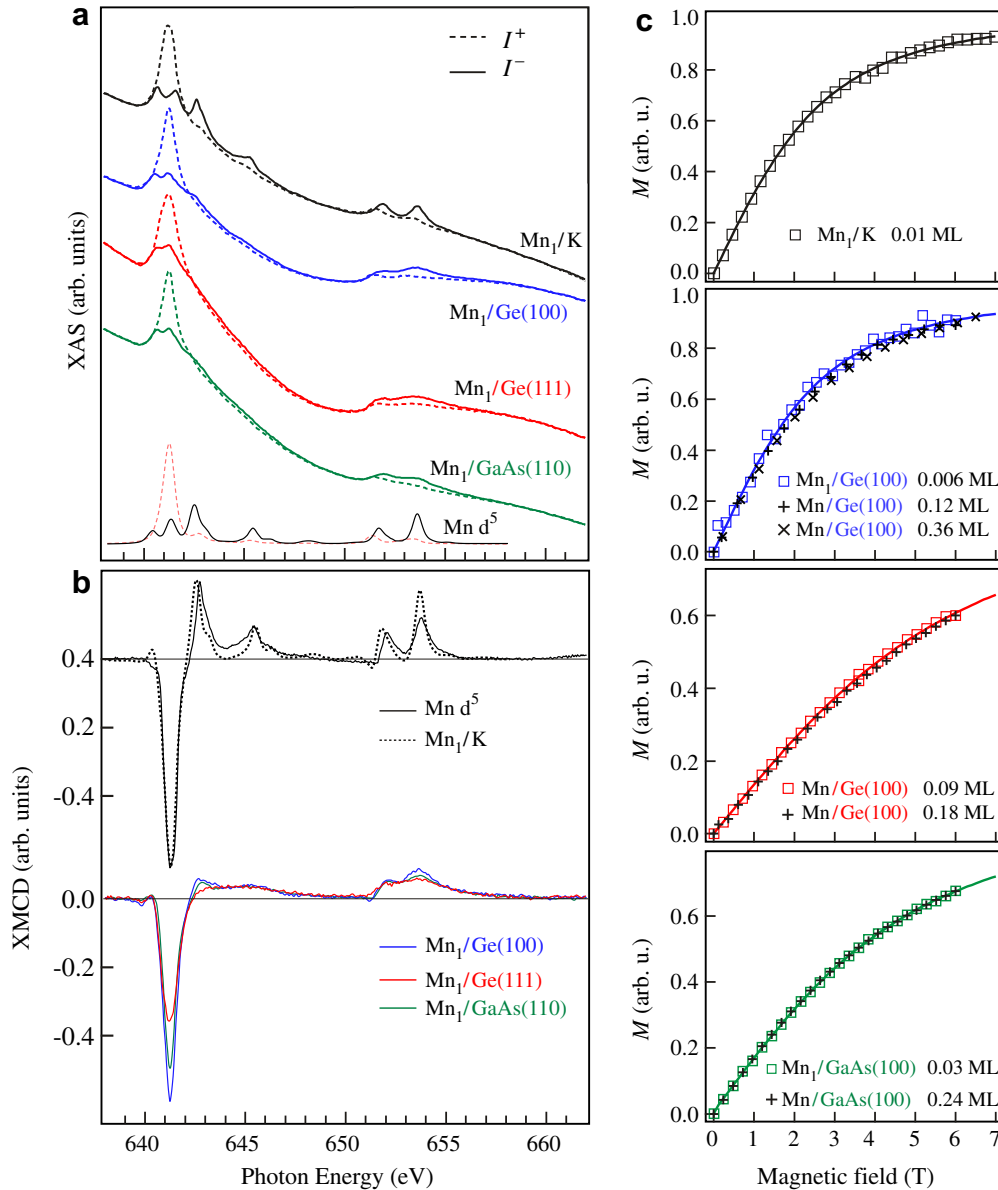


Fig. 5. (a) I^+ , I^- absorption spectra of individual Mn impurities on K, Ge(100), Ge(111), and GaAs(110) surfaces. The Mn coverage is 0.01, 0.03, 0.02, and 0.03 ML, respectively, $T = 5$ K, $B = 6$ T. (b) $I^- - I^+$ spectra scaled to the $I^+ + I^-$ intensity integrated over the L_3 edge. Multiplet calculations of I^+ , I^- , and $I^- - I^+$ are shown for $2p^6 3d^5 \rightarrow 2p^5 3d^6$ transitions of a fully spin-polarized d^5 atomic ground state in the limit of zero crystal field and at $T = 5$ K. (c) Magnetization of Mn/K, Mn/Ge(100), Mn/Ge(111), and Mn/GaAs(110) as a function of applied field and coverage. The solid lines represent fits to the lowest coverage data according to a Brillouin (Mn/K, Mn/Ge(100)) or Langevin function (Mn/Ge(111), Mn/GaAs(110)). The magnetization units are scaled to the saturation magnetization derived from the fits. Adapted from [13].

nonmagnetic Mn species. The magnitude of the XMCD effect relative to the XAS signal, moreover, shows that individual Mn impurities are strongly magnetic compared to Mn in $(Ga_{1-x}Mn_x)As$ films, where a much smaller dichroism is observed [73–76,83]. Further, the $I^- - I^+$ amplitude scaled by the L_3 absorption intensity $\int_{L_3} (I^+ + I^-) dE$ (Fig. 5b) indicates that the Mn magnetic moment is different on Ge(100), Ge(111), and GaAs(110). In particular, it is largest on Ge(100) and progressively reduced on GaAs(110) and Ge(111). The XMCD sum rules allow in principle to determine quantitatively both m_s and m_l ; however, while m_l is “safe” the derivation of m_s depends on the ability to separate the L_3 and L_2 XMCD integrated intensity, which may lead to errors as large as 50% [82,41] in the case of Mn and the lighter 3d elements, due to the reduced spin–orbit splitting of the $2p_{3/2}$ and $2p_{1/2}$ core levels. A way around this problem is discussed in Ref. [13] and relies on using the Mn/K XMCD as a reference for the known expectation va-

lue $m_s = 5\mu_B$ for the ${}^6S_{5/2}$ ground state. The values of m_s estimated in this way and the ones of m_l are reported in Table 2.

We find that, whereas m_s for Mn/GaAs(110) is close to the predicted $3.7\text{--}4.0\mu_B$ [77,78] and to the value of $4.5\mu_B$ recently derived by XMCD in Ref. [82], m_s on Ge surfaces is significantly larger than the $1.4\text{--}1.9\mu_B$ measured in Mn_xGe_{1-x} films [67]. Ab-initio calculations for bulk Mn_xGe_{1-x} consistently indicate $m_s = 3\mu_B$ and an $e_g^2(t) t_{2g}^2(t) t_{2g}^1(\downarrow)$ Mn configuration [67,79,80], arising from strong hybridization with the Ge 4p states. Interestingly, while the moment of Mn/Ge(111) is in good agreement with that calculated for bulk impurities in Ge [67,79,80] and on Ge(111) [84], Mn/Ge(100) presents a much larger m_s . This difference is attributed to the local coordination of Mn atoms on Ge(111) and Ge(100) [85]. In particular, the presence of dangling bonds on the $c(2 \times 8)$ reconstructed Ge(111) surface is likely to lead to stronger hybridization between the Mn 3d and Ge 4p states compared to Ge(100),

Table 2

Spin (m_s) and orbital magnetic moment (m_L) for ~ 0.01 ML Mn adatoms on K, Ge(100), Ge(111), and GaAs(110) derived from Fig. 5 by applying the XMCD sum rules. Total angular moment (J), and classical magnetic moment (m) obtained by fitting the Mn L_3 XMCD vs. applied magnetic field using a Brillouin and Langevin function, respectively.

	m_s (μ_B)	m_L (μ_B)	J	m (μ_B)
Mn/K	5	0	2.5	–
Mn/Ge(100)	4.8	0.07	2.4	–
Mn/Ge(111)	3.3	0.13	–	3.0
Mn/GaAs(110)	4.0	0.07	–	3.7

and to the concomitant reduction of m_s . We caution here that different adsorption sites may be occupied by Mn on semiconducting substrates, but that site-dependent magnetic moments cannot be distinguished in the present study. Both scanning tunnelling microscopy and theoretical investigations, however, indicate a strong preference for hollow adsorption sites on Ge(111) and Ge(100) [84,85], whereas large energy barriers for diffusion and subsequent incorporation prevent Mn to reach subsurface sites at low temperature. We note also that small but positive m_L (parallel to m_s) are observed, which reflect deviations from the ideal d^5 case with $m_L = 0$. The larger m_L found for Mn/Ge(111) is consistent with the increased hybridization and related broadening of the XAS and XMCD features for this surface relative to Mn/Ge(100) and Mn/GaAs(110).

Finally, we have investigated the possibility of achieving ferromagnetism limited to one or a few surface atomic layers as a function of Mn concentration, an issue of fundamental as well as practical interest to control spin-polarized electron transport across heterogeneous interfaces. We remark that ferromagnetic coupling would be expected in a Ruderman–Kittel–Kasuya–Yosida picture of hole-mediated ferromagnetism and that the radial decay of the impurity–impurity oscillatory interaction changes from $1/r^3$ in bulk to $1/r^2$ in a two-dimensional surface system. In contrast with this expectation, however, we find that all samples with coverage in the range 0.006–0.35 ML display paramagnetic behavior, independently of their extrinsic bulk doping [$2 \times 10^{18} \text{ cm}^{-3}$ n -doped Ge and GaAs, and $2 \times 10^{19} \text{ cm}^{-3}$ p -doped Ge] and despite the fact that Mn impurities typically act as acceptors in these materials. The absence of magnetic coupling even for relatively high Mn concentrations compared to bulk ferromagnetic ($\text{Ga}_{1-x}\text{Mn}_x$)As and $\text{Mn}_x\text{Ge}_{1-x}$ is thus attributed to the different electronic properties of bulk and surface semiconductors and, tentatively, to a low carrier/dopant yield, as also observed for δ -doped Mn layers in GaAs [86]. Increasing the Mn coverage at temperatures below the surface diffusion threshold leads to the statistical formation of Mn clusters of increasing size. The formation of Mn metal clusters as a function of coverage is accompanied by the decrease of the XAS-normalized XMCD signal, which indicates a reduced magnetic moment per Mn atom relative to individual impurities. By analyzing the concomitant trend of the linear dichroism signal as well as temperature annealing effects, such a decrease can be related to antiferromagnetic alignment in the Mn clusters [13]. We believe that this is also the leading cause of the magnetization deficit in bulk-like films of $\text{Ge}_{1-x}\text{Mn}_x$ and $(\text{Ga}_{1-x}\text{Mn}_x)\text{As}$.

As expected from such small orbital magnetization values, no significant magnetic anisotropy was found for the Mn adatoms. The shape of the XMCD magnetization curves in Fig. 5c thus depends only on the magnetic moment per Mn atom at a given field and temperature. Remarkably, when superposed to each other, the curves show only a very weak coverage dependence, consistent with the fact that only the Mn moment of individual or uncompensated adatoms contributes to the XMCD. We find that the curves

for Mn/K and Mn/Ge(100) can be fitted using a Brillouin function with J values of 2.5 and 2.4, respectively, which gives a magnetic moment for Mn/Ge(100) in very good agreement with the sum rule estimate. On the other hand, a Brillouin fit of Mn/Ge(111) and Mn/GaAs(110) yields magnetic moments that are a factor 3 or more smaller compared to the sum rule estimates. A Langevin fit, in this case, is in much better agreement with the sum rule moments (Table 2). As the former reflects the quantization of the angular moment expectation values and the latter the behavior of a classical magnetization vector, we may conclude, as observed also for Co/K and Co/Pt(111), that increasing the adatom–substrate hybridization also means a stronger tendency of the magnetic moment to behave in a classical way.

3. Magnetism of individual surface adsorbed atoms probed by STM

Since very recently, STM has become a mature technique for the quantitative study of the magnetism of individual atoms adsorbed on surfaces. The present section gives an account of the evolution of this technique, from the first observations of the signatures of magnetism of individual adatoms, to the quantitative determination of their effective spin moments, exchange, and anisotropy energies.

We start this section with the detection of magnetism by transport measurements through atomic point contacts. The results suggest that the spin degeneracy of the two conductance channels is lifted for magnetic atoms (Section 3.1). We then describe STM experiments where the LDOS features caused by the strong effect of magnetic impurities on superconductivity were explored, first with magnetic atoms placed on single crystal surfaces of superconductors, and second with superconducting tips approaching magnetic atoms adsorbed on normal samples (Section 3.2). The first STM measurements successful in quantifying the magnetic properties of adatoms are very recent. Magnetic anisotropy and exchange coupling energies with the neighbors in atomic chains have been deduced from the energies of spin excitations in inelastic electron tunneling spectroscopy (IETS) and are described in Section 3.3. Entire magnetization curves could be recorded over single atoms with spin-polarized (SP) STM (Section 3.4). Most recently, the combination of IETS and LDOS measurements has been used to reveal the role of magnetic anisotropy in the Kondo effect (Section 3.5). Our review of these examples intends to illustrate how the initial satisfaction to detect signatures of magnetism in atoms with the STM has now been replaced by the capacity of quantifying the effective spin, the anisotropy energies, the magnetic ground and excited state configurations, and of measuring entire magnetization curves. This evolution of STM as a sensor of atomic magnetism moves on rapidly and is expected to make significant contributions to our understanding of quantum magnetism, of magnetic impurities in solids and on thin films such as graphene, of molecular magnets, and of the magnetism of nanostructures in general.

In the literature, ample account has been given of the detection of Kondo signatures of individual atoms with the STM [87,88]. We therefore restrict ourselves to describe how these experiments are performed and refer to the literature for the most recent examples [89]. The differential conductance dI/dV is recorded at low temperature and with the STM tip positioned at constant height over the magnetic atom. To a good approximation, dI/dV can be associated with the sample LDOS which shows a sharp resonance at E_F if the atoms are Kondo screened. This resonance has been observed in photo-electron spectroscopy (PES) [90–92]. However, due to interference between electrons tunneling between substrate and tip and between adsorbate and tip, a Fano line shape results in the STM spectra [17,18]. The spatial resolution of STM enables to

study the lateral extent of the Kondo cloud and the effect of the atomic environment onto the Kondo features, whereas angle-resolved (AR) PES has the advantage of \mathbf{k} -resolution, which the STM can only achieve for the in-plane components of \mathbf{k} by looking at quantum interference patterns of surface state electrons scattering off impurities or steps [93–95].

The spin polarization of a single atom can in principle be measured with STM by means of Andreev reflection, as done for ferromagnets in mesoscopic point contacts with superconductors [96,97]. Single [98,99] and multiple [100] Andreev reflections have been observed with the STM. However, this has so far not been used to study single magnetic atoms, we therefore refer the reader to the literature also on this subject.

3.1. Transport in single magnetic atom point contacts

Magnetic atoms or molecules are expected to lift the spin degeneracy and therefore to exhibit characteristic transport properties when placed into atom point contacts distinguishing them from nonmagnetic species. After an introduction to quantized conductance we describe experiments performed by L. Bürgi in the laboratory of D. Eigler showing conductance through a single spin channel for Gd/Cu(100) [101]. This observation is in accordance with a calculation finding fully lifted spin degeneracy for ferromagnetic ballistic contacts [102].

The conductance $G = \sigma A/L$ of a wire with cross section A and length L becomes ballistic and reaches a finite value for $L < L_m$ and $L < L_\Phi$, where L_m denotes the mean free path and L_Φ the phase relaxation length of electrons in the solid of interest [103]. The finite value is an integer multiple of the quantum of conductance $G_0 = 2e^2/h$. This can be derived by assuming a free-electron gas confined in a wire along z by a potential $U(x,y)$. Since the potential does not vary along z the solutions of the Schrödinger equation are transverse modes i , denoted by quantum numbers (n_x, n_y) , each of them creating a separate subband with free-electron dispersion along k_z , which we call k for simplicity. Upon connecting this gas to two ideal reservoirs with potential difference V , each mode carries a current $I_i = e(eV\rho_i(E_F))v_{g,i}(E_F)$. The group velocity $v_{g,i}(E)$ cancels out since the density of states of a 1D free-electron gas is given by $\rho_i(E) = 2m/\pi\hbar^2 k_i(E) = 2/hv_{g,i}(E)$, and one finds the simple expression

$$G = \frac{1}{V} \sum_i I_i = \frac{2e^2}{h} N = NG_0, \quad (2)$$

where N is the number of modes for which $E_i < E_F$. A magnetic impurity may lift the spin degeneracy in the mode energies such that modes close to E_F may be moved above E_F for one spin channel such that the current is entirely carried by the other spin channel leading to a conductance per transverse mode of only $G_0/2$.

From Eq. (2) one expects conductance plateaus to appear for a contact with increasing lateral dimension, each time new transverse modes cross E_F . However, a necessary condition for the plateaus to be observed is that the lateral dimension of the contact is of the same order of magnitude as the Fermi wave length λ_F , otherwise scattering smears out the conductance steps.

Quantized conductance has been reported in experiments where the high-mobility 2D electron gas (2DEG) located at semiconductor interfaces has been constricted by gate electrodes [104,105]. For these systems L_Φ and L_m reach μm values and $\lambda_F \sim 500 \text{ \AA}$. Therefore quantized conductance becomes apparent in relatively large constrictions, implying very small transverse mode energy separations $\Delta E < 1 \text{ meV}$ necessitating sub-Kelvin temperatures for them to be resolved. In metals $\lambda_F \sim 3 \text{ \AA}$ requires atomic size constrictions for conductance quantization to be observed, but offers several eV level spacings and enables observation

of quantized conductance at room temperature. This has been realized in metallic break-junctions [106–109] even in classroom experiments [110]. However, the conductance steps for $N > 1$ were often observed at non-integer values of G_0 and their height varied significantly between subsequent experiments. Both observations were explained by a combination of STM and atomic force microscopy (AFM) revealing that conductance steps beyond G_0 were always accompanied by irreversible atomic rearrangements of the contact [111,112]. Conductance measurements in junctions between STM tips and the atomic terraces of single crystal metal surfaces revealed the transition from tunneling to quantized conductance [112–116], however, this transition was abrupt as it has been accompanied by irreversible atomic rearrangements when G_0 was reached [117], similar to the observations in break-junctions [118]. This “jump to contact” leads to ill defined restriction geometry.

Well defined single atom contacts with fully reversible electrical conductance changes could be achieved in low temperature STM experiments making contact to isolated atoms adsorbed onto single crystal terraces. Reversible opening and closure of such contacts has first been demonstrated for Xe atoms adsorbed onto a Ni(110) surface contacted by a W tip with an apex onto which a Xe atom has been transferred from the sample [114]. The resistance across the resulting two Xe atom “wire” leveled off at $10 \text{ M}\Omega$. This high value compared to $G_0^{-1} = 12.9 \text{ k}\Omega$ was explained by conductance through the Xe 6s resonance lying far above E_F .

The first reversible transition from tunneling to contact between single metallic atoms has been observed for a Au tip approaching a Mn atom adsorbed onto Cu(100) [101]. The blue curve in Fig. 6a shows the conductance trace upon approaching the tip to the sample starting from the gap resistance of $R_t = 1.29 \text{ M}\Omega$, where the tip has been stabilized before opening the feed back loop and defining $z = 0 \text{ \AA}$. The conductance increases exponentially with a slope corresponding to a tunnel barrier of about 4 eV, as expected for clean metal electrodes. The curve flattens smoothly out at z_c , from where the conductance takes on a constant value very close to G_0 . The conductance trace for retracting the tip is shown in red and perfectly overlays with the one recorded during approach. Reversibility is further proven by the constant current images in the inset recorded before and after having performed conductance measurements up to point contact on both the Mn and the Gd atom. The apparent heights and positions of the atoms did not change which is strong evidence for the absence of any atomic rearrangements on tip and sample. Reversible and smooth transitions from tunneling to one quantum of conductance were also reported for W-tips on Ag/Ag(111) and Cu/Cu(111) [115].

The conductance traces in Fig. 6b show electrical transport through two Mn atoms in series, one adsorbed onto the Au tip and the other on the Cu(100) surface [101]. Again, there is a smooth transition from tunneling to point contact. The different colors stand for different atomic configurations at the Au tip apex before adsorbing the Mn atom onto it. The tip dependence was found to be reduced significantly for two Mn atoms in series compared to contacts from the Au tip directly to the Mn adatom [101]. The plateau has an average value of $(0.95 \pm 0.04)G_0$. The most obvious interpretation of this result is that there is exactly one spin degenerate conductance channel with almost perfect transmission. Break-junction measurements and STM experiments where tip-sample necks have been opened found the number of current carrying modes of one-atom contacts to be determined by the number of available valence orbitals [109]. There are 7 in the case of Mn but the data in Fig. 6b are suggestive of 6 contributing very little or not at all, while one being the main and almost perfect channel. Conductances very close to G_0 have also been reported for reversible and well defined atomic STM contacts on Ag, Au, Cu, and Co ada-

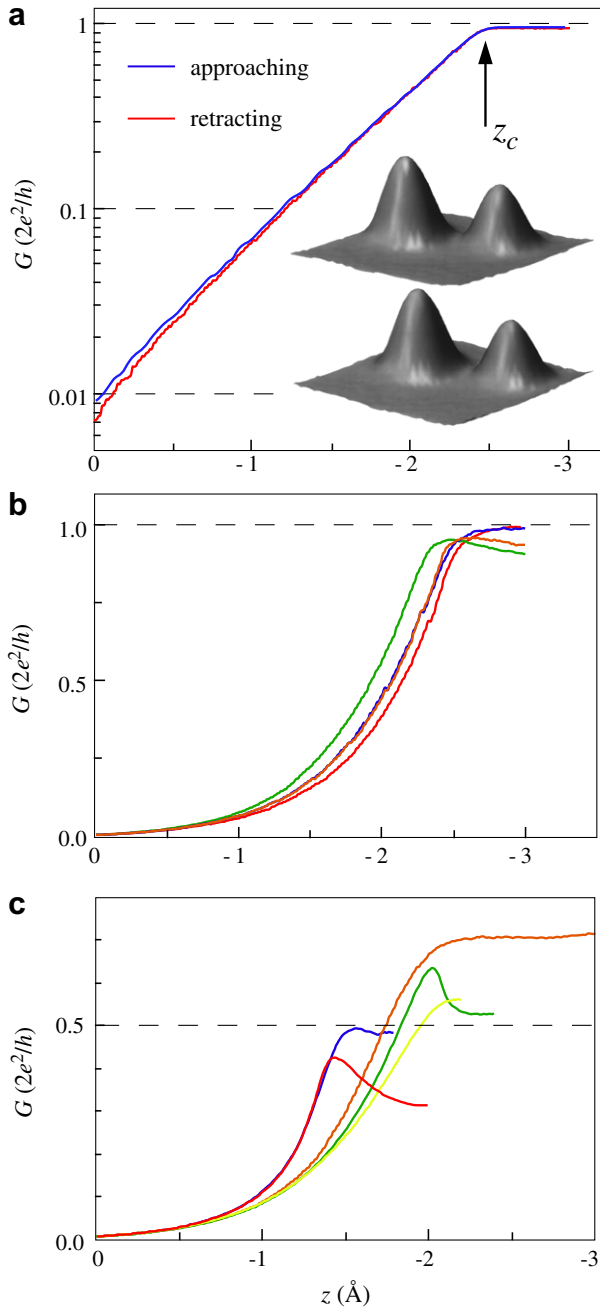


Fig. 6. (a) Electrical conductance during reversible closure and opening of a point contact between a Au STM tip and a Mn atom adsorbed on Cu(100). Inset: constant current STM images of Gd and Mn adatoms recorded before (top) and after (bottom) conductance measurements on both atoms ($36 \text{ \AA} \times 36 \text{ \AA}$, apparent heights $\Delta z_{\text{Gd}} = 2.2 \text{ \AA}$ and $\Delta z_{\text{Mn}} = 1.5 \text{ \AA}$, $V_t = 0.1 \text{ V}$, $I_t = 1.0 \text{ nA}$). (b) Conductance through an atomic junction of two Mn atoms, the first being adsorbed at the tip apex and the second on a Cu(100) surface. (c) Conductance traces with a Au tip centered over a Gd atom on Cu(100). (b) and (c) Traces with different atomic configurations at the tip apex are displayed in different colors. In all cases $z = 0 \text{ \AA}$ corresponds to a gap resistance of $1.29 \text{ M}\Omega$ and the conductance is recorded by monitoring $I_t(z)$ at $V_t = 2.58 \text{ mV}$ and $T = 5.6 \text{ K}$. From [101].

toms [119]. This strongly suggests the idea of a single conductance channel with almost perfect transmission irrespective of the chemical identity of the metal atom in contrast with the main conclusion of Ref. [109]. Attempts to enhance the conductance beyond this value lead to atomic rearrangements [101].

Conductance traces of a junction formed by a Gd atom adsorbed onto Cu(100) and a Au tip (Fig. 6c) level off at significantly lower

plateau values [101]. An average over 10 traces yields $(0.52 \pm 0.10)G_0$ which is very close to half the quantum of conductance. However, there is significant scattering of the plateau values and of the shape of the traces for different microscopic tip geometries. Due to time limitations the measurements were recorded only with a Au tip. It would have been interesting to see whether the scattering around $G_0/2$ would have been reduced for two Gd atoms in series, as in the case of Mn. Seen that all adatoms other than Gd had conductances very close to G_0 and therefore one spin degenerate channel with almost perfect transmission, it is unlikely that Gd has spin degenerate transport with a transmission of only $1/2$. It is much more plausible to attribute this finding to spin-polarized transport caused by the $4f$ magnetism of Gd lifting the spin degeneracy and thus leading to conductance through only one spin channel.

In contrast to Gd, conduction through Co adatoms did show values very close to G_0 and not $G_0/2$ [119,120]. The substrates used for the Co conductance traces were Cu(111) and Cu(100), which both show Kondo screening with Co. The Kondo signatures prevail up to contact, as seen in dI/dV -curves recorded in contact [119,120], whereas such curves on Gd showed perfect Ohmic behavior [101]. The adsorption complex composed of the Co adatom and its screening cloud in the substrate forms a nonmagnetic many-body singlet ground state around E_F and therefore lifting of spin degeneracy is not expected, while the unscreened magnetism of Gd does seem to lift the spin degeneracy. More measurements are needed to ascertain this signature of magnetism in transport across magnetic atoms adsorbed onto surfaces.

3.2. Subgap states caused by magnetic atoms in proximity of superconductors

Low lying bound quasiparticle excitations with electron-hole asymmetry are distinctive signatures of magnetic impurities in superconductors and can therefore be used to identify magnetism of single magnetic atoms in contact with or in close vicinity of a superconductor.

The strong effect of magnetic impurities on superconductivity manifests itself by the large reduction of the transition temperature T_c caused by a reduction of the order parameter around the impurities leading to the appearance of quasiparticle excitations within the gap [121]. Such excitations have first been observed in planar tunnel junctions doped with magnetic impurities [122,123]. In such spatially averaging measurements, the electron-hole asymmetry vanishes and the features in the local density of states (LDOS) become symmetric with respect to E_F , leading to the name mid-gap states.

The first spatially resolved measurement of the effect of magnetic impurities on the superconducting DOS has been reported from low- T STM experiments with Au tips on a Nb(110) surface [16]. Fig. 7a shows differential tunneling conductance measurements which can be associated with the quasiparticle LDOS of the sample since tips with a featureless LDOS close to E_F were used. The spectrum over clean Nb(110) shows a gap which is perfectly fitted by thermally broadened ($T = 3.85 \text{ K}$ in agreement with the microscope operating temperature of $T = 3.8 \text{ K}$) BCS density of states yielding a gap of $\Delta_{\text{surf}} = 1.48 \text{ meV}$ very close to the bulk value of $\Delta_{\text{bulk}} = 1.53 \text{ meV}$ ($T_{c,\text{bulk}} = 9.3 \text{ K}$). Near magnetic impurities the authors observed quasiparticle excitations inside the gap, which were localized at a radius $r < 12 \text{ \AA}$ around the impurity. These are far shorter length scales than the superconducting coherence length of $\xi_0 = 390 \text{ \AA}$. The Mn induced bound states are best seen in the difference spectrum shown in Fig. 7b. There is an overall enhancement of the LDOS which is clearly asymmetric with respect to E_F . It has its maximum intensity for the tip centered above the Mn atom. Gd adatoms showed similar LDOS features within the

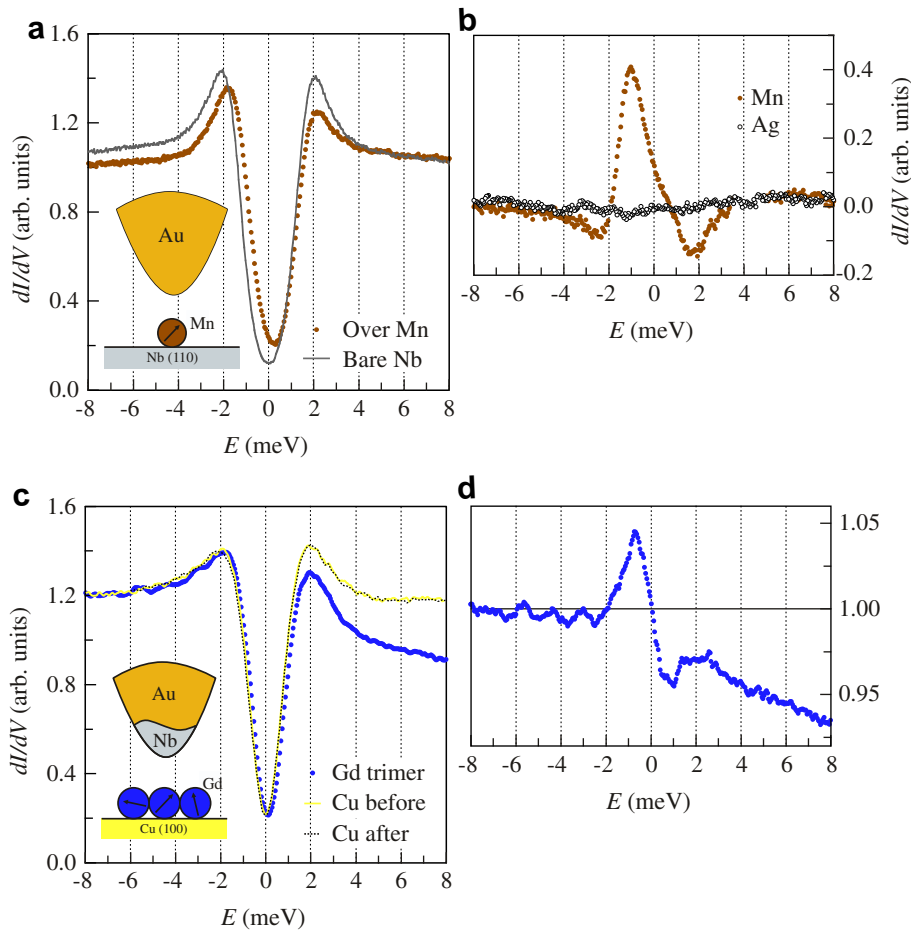


Fig. 7. (a) Scanning tunneling spectra recorded with a Au tip once over bare Nb(110) and once centered above a Mn adatom. (b) Difference spectrum between bare Nb(110) and Mn shows asymmetric bound state which is absent for Ag. Tip stabilization at $V_t = 10$ mV, $I_t = 1.0$ nA, $T = 3.8$ K, from [16]. (c) Spectra taken with a superconducting Nb cluster at the apex of a Au tip over a Gd trimer adsorbed on Cu(100) compared with the reference spectra over bare Cu(100) taken before and after the Gd trimer spectrum. (d) Spectrum over Gd trimer divided by reference spectrum showing again bound state, this time due to the magnetic cluster in proximity of the superconducting tip. Tip stabilization at $R_t = 2$ M Ω , modulation amplitude $V_{mod} = 0.35$ mV for Lock-in detection of dI/dV , $T = 5.6$ K, from [101].

gap, however, with inverted asymmetry and with the maximum intensity localized at $r = 6$ Å off the impurity center. As Fig. 7b shows, Ag adatoms on Ni(110) have no LDOS features in the gap, as expected for ostensibly nonmagnetic atoms.

The Mn induced LDOS in the superconducting gap could be reproduced within a model introducing a spin-dependent exchange potential J and an ordinary scattering potential U , both having non-zero values inside a radius a around the impurity. The order parameter was assumed to vanish for $r < a$ and to take on the Nb bulk value outside. The most important parameter is J as it breaks the time-reversal symmetry between electron and hole-like states and therefore produces the experimentally observed asymmetry. The best agreement with the difference spectrum of Fig. 7b was achieved for $J = 4$ eV and $a = 2.5$ Å. Variations of U from 0 to $0.15 E_F$, together with variations of J by $\pm 5\%$ around 4 eV, did all fit the data equally well. Therefore J is well determined by the experiments, while U is not. Note that J can only be retrieved from the local measurements, since only they reveal the asymmetry. Spatial averaging of the tunneling spectra over the surface spot where the impurity showed its effect removed the asymmetry, in agreement with observations from planar junctions. Bound state excitations have also been observed in STS measurements on Ni impurities located near the surface of a high- T_C superconductor, where magnetic impurities have been proposed to contribute to superconductivity, rather than to quench it [124].

The detection of individual magnetic atoms adsorbed on the surface of a normal metal has been achieved by inverting the above configuration of the electrodes [101]. For this purpose, Au tips with a superconducting Nb cluster at their apex have been prepared, and their superconducting properties have been characterized by recording dI/dV -curves on normal and on superconducting surfaces. The spectra in Fig. 7c show the symmetric and thermally broadened BCS gap ($\Delta_{tip} = 1.2$ meV) of such a tip over Cu(100), together with an asymmetric spectrum recorded with the very same tip above an adsorbed Gd trimer. Tip changes between the two spectra can be excluded, since the control spectrum recorded afterwards on Cu(100) is identical to the one before. Fig. 7d shows the $Gd_3/Cu(100)$ spectrum divided by the reference spectrum. It clearly reveals the asymmetric subgap features reminiscent of magnetic impurities in proximity of a superconductor. Test experiments with the Gd trimer on a superconductor (Nb(110)) and a superconducting tip (Au wire with a Nb cluster on the apex) showed that the Gd_3 -related LDOS features became more and more symmetric as the tip was approached, until an entirely symmetric spectrum was obtained at $R_t = 500$ k Ω [101]. At that point the effect of the magnetic impurity on both electrodes became identical proving that an STM tip can be brought in sufficient proximity to a magnetic impurity to induce the same effects as if the impurity was adsorbed directly onto it. Therefore the subgap features in Fig. 7d can unequivocally be attributed to the magnetic moment

of the Gd trimer. According to Fig. 7b no such features are observed for nonmagnetic atoms. Note that similar to the quantized transport measurements discussed above, no signatures of magnetism are observed in superconductors in proximity of magnetic impurities which are Kondo screened. The difference spectra obtained with Nb-tips above Co/Cu(111) showed asymmetric dips which were perfectly described by a Fano function [89], and the spectrum for Co/Ag(100) could be fitted by combining a BCS LDOS with a Fano function [125].

There are several ways to prepare superconducting STM tips. For instance, PtIr-tips have been covered by Pb layers and then capped by proximity coupled Ag thin films [126], but also etched or machined bulk Nb [127], Al [128], and Pb [98,128] tips have successfully been used. It has been shown that STM tips may remain superconducting up to higher magnetic fields than bulk critical fields [129]. Altogether, this encourages the use of superconducting tips for the detection of magnetism through the induced asymmetric bound states. In addition, they may be used as source for spin-polarized electrons [130,131]. Theoretically, a 100% polarized electron source could be created by adsorbing a magnetic impurity onto a superconducting tip. Depending on the magnitude of the exchange potential J the electronic spin of the subgap excitations can be parallel or anti-parallel to the one of the magnetic impurity [132–134]. If this impurity has a stable moment it would act as a stable source of polarized electrons at the excitation energy. This has first been proposed in Ref. [101] and realized in Ref. [89], but unfortunately on a Kondo screened magnetic impurity calling for repetition of this experiment on unscreened magnetic impurities. A final promising application of superconducting tips are scanning Josephson junctions, e.g., for the study of lateral variations of the superconducting order parameter.

3.3. Spin excitation spectroscopy with the STM

The group of A. Heinrich constituting the low- T STM lab founded by D. Eigler at IBM Almaden has pioneered spin excitation spectroscopy as a tool to quantify the magnetic properties of individual atoms or clusters [20,135,21]. The technique relies on inelastic scanning tunneling spectroscopy (ISTS) measuring excitation energies with high lateral resolution and is inspired by inelastic electron tunneling spectroscopy (IETS) work on planar tunnel junctions [136,137]. The excitations can be vibrations [138] or changes in the magnetic state of atoms or molecules in the tunnel junction [20,135,21], as well as surface magnons [139]. With increasing tunnel voltage one observes a conductance step each time the tunneling electrons reach the threshold energy needed to excite the system since this opens a new inelastic conductance channel. For magnetic atoms, the energies and amplitudes of the conductance steps deliver valuable information on their magnetic ground state and anisotropy, and in the case of clusters also on the Heisenberg exchange coupling between the atoms in the cluster. Finally, the symmetry of the curves about E_F bears information on the spin polarization of the tip.

The first ISTS steps stemming from spin excitations were reported [20] for Mn atoms in an external magnetic field and adsorbed on the self-limiting $\text{Al}_{10}\text{O}_{13}$ -layer formed by oxygen exposure of a NiAl(110) surface [140]. Due to the small energies involved, the measurements had to be performed at 0.6 K. The step energies were proportional to the magnetic field, $E_{\text{step}} = g\mu_B \mathbf{B}$, yielding the Landé g -value for Mn atoms as a function of their adsorption site. The results were close to the free-electron value of 2.0023, with 5% variations caused by the atomic environment of the Mn atoms. The amplitudes of the conductance steps were very sensitive (20–60%) to the atomic environment. Mn atoms adsorbed directly onto NiAl(110) did not show the steps, signifying

that either the insulating layer is needed to enhance the cross section for spin scattering, or that the Mn spin is modified by stronger hybridization due to direct adsorption on the metal surface.

The spin excitation steps were also found placing the Mn atoms on a different ultrathin insulator, namely on a $\text{Cu}_2\text{N}-c(2 \times 2)$ -layer on Cu(100) [135]. Fig. 8a shows an STM image of square Cu_2N -islands coexisting with clean Cu rims appearing as narrow vertical and wider horizontal ridges. The island pattern is typical for chemisorbed N on Cu(100) [141]. The island size is determined by an optimum between strain and edge energy and they order by long-range elastic interactions mediated by the substrate [142]. The insets in Fig. 8c and d show the topview of the $c(2 \times 2)$ -structure. DFT-calculations show that the N atoms are almost at the same height as the first atomic Cu plane [21]. One therefore speaks of a Cu_2N -layer rather than of a N/Cu(100)- $c(2 \times 2)$ adlayer.

Vertical atom transfer [143,144] was used to assemble straight Mn_n chains with the STM. The chains displayed a striking parity dependence in their ISTS steps. Chains with even number of atoms n had no step close to 0 eV but large steps at several meV energy, while chains with odd n displayed zero-energy steps together with less pronounced ones at higher energy. The absence of low-energy spin excitation in even chains implies a ground state with $S = 0$ and their presence in odd chains an $S \neq 0$ groundstate. Therefore the chains were anti-ferromagnetic (AF) and hence a realization of Heisenberg chains with finite length [145]. In contrast to Mn on alumina, the zero-energy step of Mn atoms and odd chains was observed in the absence of an external magnetic field, which was interpreted as a signature of magneto-crystalline anisotropy. The dimer conductance steps split up into three in an external magnetic field. Accordingly, they were attributed to transitions from the $S_{\text{tot}} = 0$ singlet to the $S_{\text{tot}} = 1$ triplet state with quantum numbers $m = 0, \pm 1$. The step positions were used to derive the exchange energy $J = 6.2$ meV from a Heisenberg Hamiltonian. As discussed above for the Landé values, also the coupling strength varied for different locations on the Cu_2N -island (by $\pm 5\%$); placing the whole chain on N instead of Cu adsorption sites led to $J = 3.0$ meV. The spin per Mn atom could be inferred from the position of the IETS step of Mn_3 to $S = 5/2$ which is also the spin of a free Mn atom. From the known J and S values the spin transitions for all chain lengths can be derived from a Heisenberg open-chain model and the values were in excellent agreement with experiment for chain length up to 6 atoms. From the fact that the trimer steps did not split up in a magnetic field, the following empiric IETS-selection rules were established. Conductance steps appear for $\Delta S = 0, \pm 1$ and $\Delta m = 0, \pm 1$, but not for $\Delta m = \pm 2$. These experiments illustrate how textbook examples of low-dimensional magnetism, such as finite Heisenberg chains, can be assembled and studied by means of STM.

The adsorbates visible in Fig. 8a are Fe, Co, and Mn atoms. Spectra taken on an Fe atom adsorbed onto a Cu site on Cu_2N are shown in Fig. 8b at zero magnetic field and in Fig. 8c and d at finite fields along the two non-equivalent in-plane directions. In Fig. 8b there are three with respect to E_F symmetric pairs of inelastic excitation steps located at 0.2, 3.8, and 5.7 meV. The finding of multiple steps for a single atom can only be rationalized by a high spin ($S > 1/2$) subject to magneto-crystalline anisotropy. The spin-Hamiltonian reads with the nomenclature of molecular magnets

$$\hat{H} = g\mu_B \mathbf{B} \cdot \hat{\mathbf{S}} + D\hat{S}_z^2 + E(\hat{S}_x^2 - \hat{S}_y^2). \quad (3)$$

After the Zeeman energy, the second and third terms represent the axial and transverse anisotropies D and E , respectively. The assignment of the axes is by convention such as to maximize $|D|$ and to yield $E > 0$. By diagonalization of Eq. (3) one finds the eigenvectors and the spin excitation spectrum. Under the assumption of a spin $S = 2$ all step positions for different field values and direc-

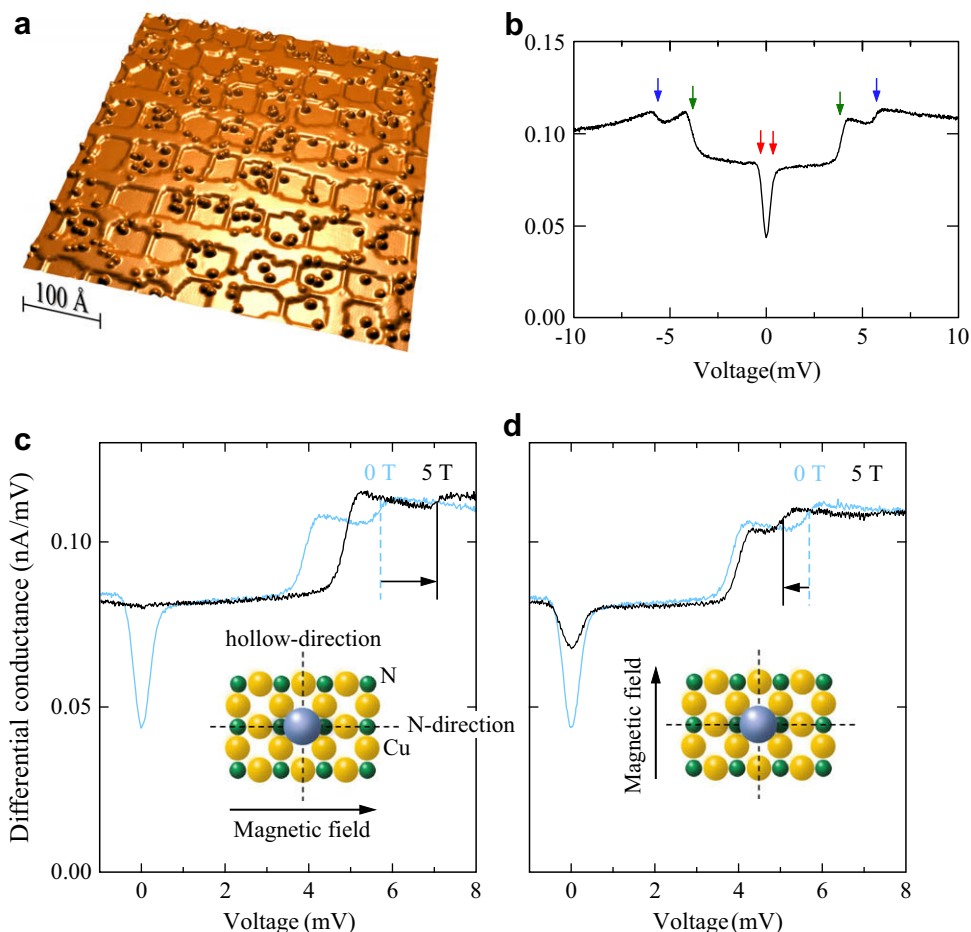


Fig. 8. (a) Constant current STM image showing square Cu_2N -patches with a $c(2 \times 2)$ structure on $\text{Cu}(100)$ appearing lower than the coexisting bare Cu ridges. The adatoms are Fe, Co, and Mn and can be discerned by their characteristic spectroscopic features and apparent heights ($500 \text{ \AA} \times 500 \text{ \AA}$, $V_t = 10 \text{ mV}$, $I_t = 0.5 \text{ nA}$, $T = 5 \text{ K}$). (b) Spectrum over Fe atom adsorbed on a Cu site of Cu_2N . Each time the electron energy reaches the threshold needed for an allowed transition of magnetic eigenstates, the differential conductance abruptly increases (tip stabilization at $V_t = 10 \text{ mV}$, $I_t = 1.0 \text{ nA}$, $V_{\text{mod,rms}} = 20 \text{ \mu V}$, $f_{\text{mod}} = 800 \text{ Hz}$, $T = 0.5 \text{ K}$). Magnetic fields applied along the N-direction (c) shift the magnetic excitation energies in a different way than fields along the hollow direction (d), from [21,168].

tions could perfectly be fitted by $g = 2.11 \pm 0.05$, $D = -1.55 \pm 0.01 \text{ meV}$, $E = 0.32 \pm 0.01 \text{ meV}$ and with z along the N-direction. The negative value of the axial anisotropy D signifies that a large projection of the spin onto the z -axis is favored, *i.e.*, Fe atoms have easy axis anisotropy on this surface. In order to compare D with the uniaxial anisotropy K , used in bulk, thin films and nanostructures and referred to in Section 2, one has to multiply D by S^2 and thus obtains anisotropies almost as large as the ones of $\text{Co/Pt}(111)$ [11]. Easy axis anisotropy implies that the zero-field ground state has large and identical weights in the $m = \pm 2$ eigenstates. However, it is not entirely $m = \pm 2$, since the finite transverse E -term mixes states of different m .

In fact, each of the steps marked by the differently colored arrows in Fig. 8b implies more than a single change of m . Let us consider the third transition marked by a blue arrow in order to see how the wave function changes for this excitation. The step shifts up in energy when a field of 5 T is applied along the easy axis, as becomes evident from Fig. 8c. In the absence of the field, the ground state is a symmetric mixture of $m = \pm 2$, with very little weight also in $m = 0$. The electron with an energy around 6 meV can induce a transition to a state with equal weights in $m = \pm 1$ and no more weight in $m = 0, \pm 2$. Therefore S_z^2 gets reduced to zero, *i.e.*, in a classical image the moment gets fully turned away from the easy axis. The energy required for this is $K = D S^2 = 6.2 \text{ meV}$, as observed. The field breaks the symmetry along z and favors

$m = -2$, and an electron can make a transition to $m = -1$, but also from the non-zero $m = 0$ and $m = 2$ components of the wave function to $m = 1$ and from $m = 0$ to $m = -1$. This time, the excited state is not symmetric and has more weight in $m = 1$. Classically, this corresponds again to tilting the moment away from the easy axis, but this time it is even slightly reversed, shifting up the step by more than 1 meV. Applying the field along the transverse direction favors a reduction of S_z and therefore the very same step gets shifted to lower energy in Fig. 8d. Knowing the eigenvalues in ground and excited states also gives a clear picture of the selection rules. Only transitions with $\Delta m = 0, \pm 1$ are allowed, consistent with the electron being able to transfer a spin of one when inverting its own spin. Also the step heights can be rationalized. For example, the first excitation step disappears in Fig. 8c as the field is applied. For this step the wave function changes from Ψ_0 with most weight $m = -2$ to Ψ_1 with most weight in $m = 2$. Therefore it essentially corresponds to spin reversal being only linked by the weak weight in $m = 2$ before and in $m = -2$ after the excitation which makes the peak disappear. DFT-calculations confirm the choice of $S = 2$, but also show that Fe pushes the underlying Cu atom deep below the first atomic plane and therefore Fe forms an adsorption complex with the neighboring N atoms and the underlying Cu, having similarities with the configuration in molecular magnets [21]. As opposed to molecular magnets, in $\text{Fe/Cu}_2\text{N}$ quantum tunneling of the magnetization is not allowed since in-plane anisotropy has or-

der 4 and there are by symmetry no transverse terms. The same analysis has been performed for Mn which again has easy axis anisotropy, however, this time out-of-plane and with $D = -0.039 \pm 0.001$ meV a much smaller value ($S = 5/2$, $g = 1.90 \pm 0.01$, and $E = 0.007 \pm 0.001$ meV).

The examples illustrate how quantitative information on the magnetic quantum states of single atoms adsorbed onto surfaces can be gained with spin excitation spectroscopy. The insulating layers have been used to enhance the cross section but are not necessary by any physical principle for the spin excitations to occur. Therefore spin excitation ISTS might in the future also address magnetic atoms adsorbed directly onto metal surfaces and therefore establish the link with XMCD results. On the other hand, XMCD measurements addressing Fe/Cu₂N/Cu(100) have been performed and are currently analyzed.

3.4. Magnetization curves taken by means of spin-polarized STM

Spin-polarized (SP) STM has been pioneered by R. Wiesendanger [146] and is now a well established technique [147,148]. Its magnetic contrast relies on the spin-valve effect. To name only a few examples, SP-STM has revealed images of spin ground states in thin films which would have been difficult to guess without spatial magnetic resolution [149], the role of adsorbates in the magneto-resistance of tunnel junctions has been addressed [150,151], and our understanding of current-induced magnetization reversal has been improved [152].

We discuss here magnetization curves recorded on single Co atoms on Pt(111) which constitutes a hallmark in SP-STM [23]. The measurements have been performed in the so-called SP-STs mode, where the differential conductance dI/dV is recorded at a given tunnel voltage as a function of the magnetic field with the tip kept at constant height and centered above the magnetic impurity. dI/dV is composed of a non-polarized (np) and a polarized (pol) part, the latter being maximized for parallel and minimized for anti-parallel alignment of tip and sample magnetization, thus one can write $dI/dV = (dI/dV)_{np} + \mathbf{M}_{tip} \cdot \mathbf{M}_{sample}(dI/dV)_{pol}$. In analogy with the polarization of the current itself, $P = (I_p - I_{ap}) / (I_p + I_{ap})$, where p denotes parallel and ap anti-parallel tip and sample magnetization, one defines a differential polarization $p = ((dI/dV)_p - (dI/dV)_{ap}) / ((dI/dV)_p + (dI/dV)_{ap})$. Co atoms adsorbed on the two non-equivalent threefold Pt(111) hollow sites have different electronic structure close to E_F [153]. Co has larger LDOS at -0.1 eV when on an hcp compared with an fcc site [23]. In order to obtain comparable magnetic contrast for the two species, the $M(H)$ -curves have been recorded at a tunnel voltage minimizing the adsorption site dependence of p , namely at $V_t = 0.3$ V. Maximum spin contrast could have been achieved at $V_t = -0.05$ V, but with a large adsorption site difference caused by the variation of the non-polarized part of the electronic structure, $(dI/dV)_{np}$.

Fig. 9a and b shows a 3D representation of constant-current STM images of individual Co atoms on Pt(111) color coded by the dI/dV -signal at 0.3 V. Indeed, all the atoms switch their magnetization upon field reversal from (a) to (b) and the differences between the atoms are small compared to this change confirming that the dI/dV -signal is dominated by magnetic and not by adsorption site contrast. As expected for magnetic tunnel junctions with soft magnetic tips, the upper $M(H)$ -curve in Fig. 9c has the shape of a butterfly, resulting from magnetization reversal of both electrodes at different fields [23]. The tips were Cr-coated W-tips which were dipped into a Co ML-film on Pt(111) in order to retain strong out-of-plane spin polarization. The schematic drawings indicate that a positive field sweep (red) starts at -2 T with the magnetization of both electrodes pointing down, at 0.1 T one turns up reducing dI/dV , until the second electrode turns up, too between 0.7 and 1.0 T recovering the initial dI/dV value which then stays

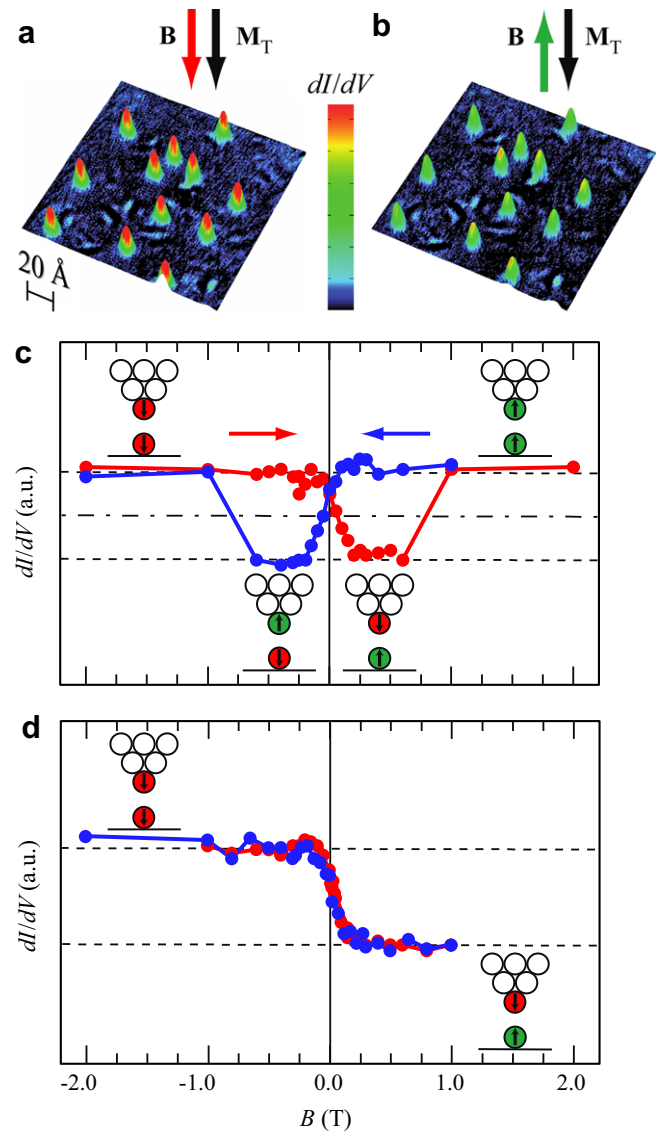


Fig. 9. (a) and (b) 3D view of constant current STM images of Co atoms on Pt(111). Color code shows magnetic contrast from dI/dV for parallel (a) and antiparallel (b) field direction and tip-magnetization ($V_t = 0.3$ V, $B_z = \pm 0.5$ T, $T = 0.3$ K). Magnetic field-dependent differential conductance of (c) soft and (d) hard magnetic tip over a Co atom on Pt(111). Red curves show up and blue ones down sweep of magnetic field ($I_t = 0.8$ nA, $V_t = 0.3$ V, $V_{mod} = 20$ mV, $T = 0.3$ K). The insets indicate the relative orientation of adatom and tip \mathbf{M} . The soft tip leads to butterfly shaped curves since it reverses its magnetization at around 0.8 T. The tip with high coercivity shows paramagnetic $M(H)$ -curves reflecting the magnetization reversal of the atoms only. The curves are shifted horizontally due to the stray field of the tip. For the soft tip the shift depends on direction of field sweep and for the hard tip there is a right shift for both sweep directions, from [23].

constant up to 2 T. The down sweep curve (blue) is symmetric with respect to the zero-field line. From reference measurements on a Co monolayer stripe on the same surface with the same tip, the electrode switching at around 0.8 T is identified as being the tip. The electrode switching at much lower fields is the Co adatom. For symmetry reasons, switching takes place at exactly half way between dI/dV_p and dI/dV_{ap} , see the horizontal lines in Fig. 9c. The atom investigated switches at ± 0.1 T. Fig. 9d shows a curve recorded with a hard tip having stable magnetization throughout the applied field sweep. The resulting paramagnetic $M(H)$ -curve is shifted slightly to the right for both sweep directions. The horizontal shifts are caused by the stray field of the tip, changing sign with field sweep direction for magnetically soft tips, while remaining

constant for the tip with high coercivity. Stray field and tip reversal can be corrected for revealing that the atoms switch reversibly at 0 T, *i.e.*, they are paramagnetic at 0.6 K.

Quantitative information on magnetic moments has been obtained from $M(H)$ -curves recorded at different temperatures and over many different Co atoms. The curves at 4.2 and 0.3 K shown in Fig. 10a are both reminiscent of paramagnetic atoms. They have been obtained by recording dI/dV -images such as Fig. 9a and b for many fields between -7.5 and 7.5 T and laterally averaging the signal over $5 \text{ \AA} \times 5 \text{ \AA}$ squares centered at the Co atoms. As expected, the saturation field increases proportional with increasing temperature. The absence of hysteresis down to 0.3 K is not expected from $K = 9.3 \pm 1.6 \text{ meV}$ [11] and has been interpreted as due to quantum tunneling of the magnetization. The full lines show that the curves can perfectly be fitted with an energy given as function of field B and its angle with respect to the atom moment m as $E(B, \Theta) = -m(B - B_{\text{tip}})\cos(\Theta) - K\cos^2(\Theta)$. With K kept at the XMCD value of 9.3 meV the essential fit parameter is m . The m -distributions recorded for about 80 Co atoms are narrow at 4.2 K and rather broad at 0.3 K ($2\mu_B \leq m \leq 6\mu_B$). Fig. 10b shows that also the saturation field strongly varies from atom to atom ($0.2 \text{ T} \leq B_{\text{sat}} \leq 0.7 \text{ T}$). In contrast, there is almost no difference in the average m -values and their variance between Co atoms on fcc and hcp adsorption sites (mean values $\bar{m}_{\text{hcp}} = 3.9 \pm 0.2\mu_B$ vs. $\bar{m}_{\text{fcc}} = 3.5 \pm 0.2\mu_B$ at 0.3 K).

The wide B_{sat} and m -distributions have been attributed to magnetic interactions between the atoms and adsorbed ferromagnetic Co stripes. Exchange energies in the order of $J = m(0.7 \text{ T} - 0.2 \text{ T})/2 = 50 \mu\text{eV}$ (with $m = 3.7\mu_B$) are needed to produce the observed variance in B_{sat} . $M(H)$ -curves of single adatoms taken as function of their distance from a Co monolayer stripe showed oscillating interactions changing from AF to FM and back to AF with increasing distance. Dipolar interactions would always be AF, and direct exchange interactions can be excluded from the large distance between the atoms. The observed oscillatory behavior with decaying strength is reminiscent of substrate mediated Ruderman–Kittel–Kasuya–Yosida (RKKY) interactions [154–156]. The interaction energy showed the expected distance dependence, $J(d) = J_0 \cos(2k_F d)/(2k_F d)^D$, with the first data points located around (14 \AA , $-180 \mu\text{eV}$) and the last one at (45 \AA , $-10 \mu\text{eV}$). Best agreement between experiment and this expression was obtained for a dimension of $D = 1$. This can be rationalized by the fact that the atoms are separated from a straight 1D interface, and integration over 2D interactions between a fixed point and points located along a straight line yield a decay close to $D = 1$. However, the wave-length was with $\lambda_F = 30 \text{ \AA}$ 2–6 times larger than typical values for Pt(111) [157].

These results show that single Co atoms on Pt(111) behave as paramagnetic impurities when placed in an STM junction biased at 0.3 V. They are subject to substrate mediated RKKY-interactions which can be detected down to $10 \mu\text{eV}$ resolution by recording the exchange field stemming from a ferromagnetic monolayer high stripe attached to a substrate step.

3.5. Simultaneous measurement of anisotropy energy and Kondo properties

It is very difficult to predict which magnetic species will display the Kondo effect in which host. A step forward was made for high spin impurities by showing magneto-crystalline anisotropy energy to play a decisive role. By analyzing spin excitations of single adatoms with ISTS, and simultaneously looking for a Kondo resonance in their LDOS, easy plane anisotropy has been found to be a necessary condition for Kondo screening of an impurity with $S > 1/2$ [158]. In addition, it was confirmed that $S = 1/2$ impurities are not at all subject to anisotropy.

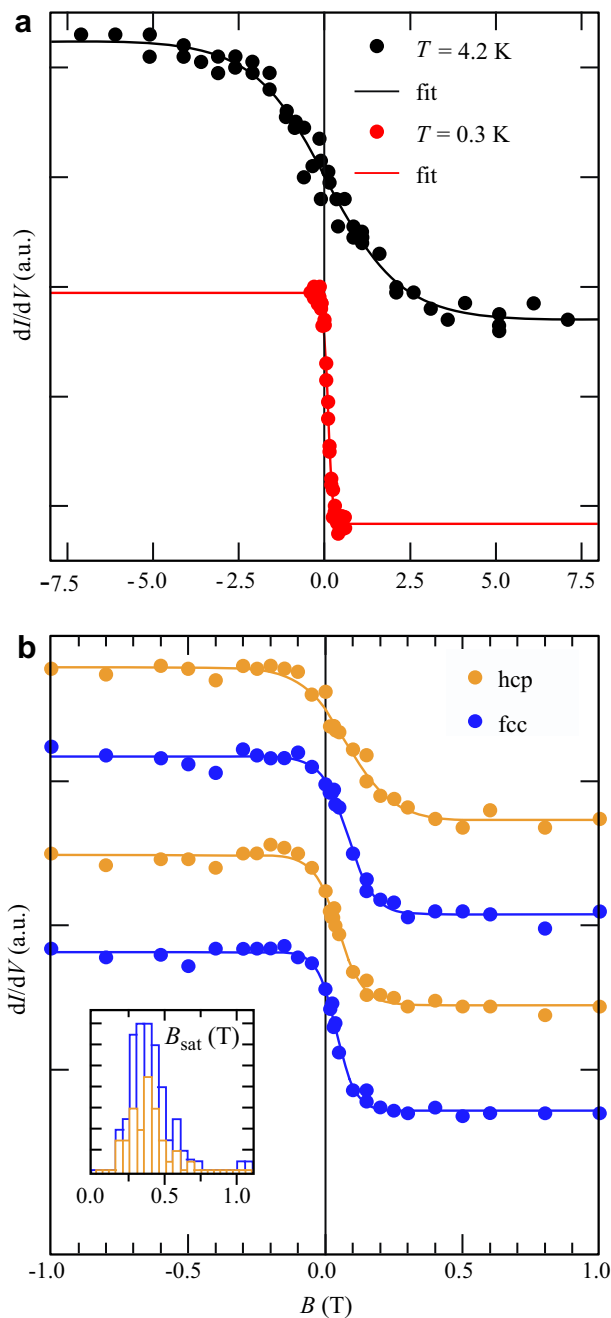


Fig. 10. (a) $M(H)$ -curves on the same atom at $T = 4.2$ and 0.3 K . Points represent experimental data, solid lines are fits according to the function described in the text. (b) $M(H)$ -curves recorded at 0.3 K on four Co atoms, two on hcp (yellow) and two on fcc (blue) sites, showing strongly differing saturation fields independent of adsorption site. Inset: histogram of 0.3 K saturation fields for the two adsorption sites. Parameters for all $M(H)$ -curves $I_t = 0.8 \text{ nA}$, $V_t = 0.3 \text{ V}$, and $V_{\text{mod}} = 20 \text{ mV}$, from [23].

Fig. 11a shows dI/dV -spectra over a Co atom adsorbed onto a Cu site on $\text{Cu}_2\text{N}/\text{Cu}(100)\text{-c}(2 \times 2)$. There are clear conductance steps at around $\pm 6 \text{ meV}$, moving inwards as a magnetic field is applied into the direction where the Co atom has two hollow sites as neighbors. Applying the field along the N-direction as well as perpendicular to the surface led to an outward shift of the steps, and this shift was comparable for both directions. From this qualitative behavior, one can conclude that Co has a high magneto-crystalline anisotropy with hard axis along the hollow direction and easy plane perpendicular to it. From a similar analysis as in Section

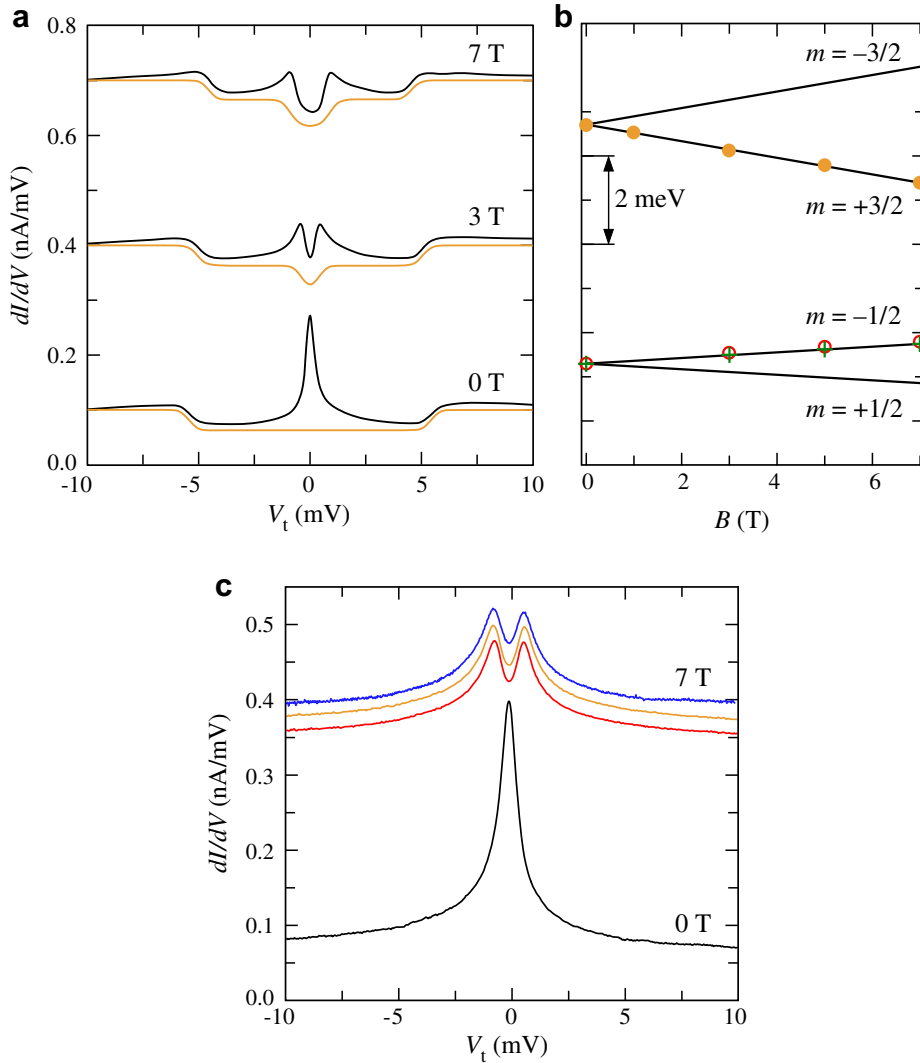


Fig. 11. (a) Differential conductance measured with STM tip centered above a Co atom adsorbed on a Cu site of $\text{Cu}_2\text{N}/\text{Cu}(100)-(2 \times 2)$. The central Kondo resonance splits for increasing magnetic field directed along the hollow-direction and the spin excitation conductance steps shift slightly inwards due to magneto-crystalline anisotropy ($T = 0.5$ K, tip stabilized at $V_t = 10$ mV and $I_t = 1.0$ nA). Yellow curves represent calculated spin excitation spectrum. (b) Field dependence of spin excitation energies for transitions from $m = 1/2$ to $m = -1/2$ and to $m = +3/2$, reminiscent of easy plane anisotropy (field along hollow-direction). (c) dI/dV for a Ti atom on $\text{Cu}_2\text{N}/\text{Cu}(100)$ showing the central Kondo resonance, but no conductance steps since Ti is a spin $1/2$ system and has no magnetic anisotropy. This is confirmed by the isotropic shifts of the Kondo resonance for the field applied along three orthogonal directions (red and yellow in-plane, blue out-of-plane). All spectra recorded with $V_{\text{mod}} = 50$ μV rms-modulation at 745 Hz and at $T = 0.5$ K, from [158].

3.3, the total spin ($S = 3/2$) and the anisotropy energy ($D = 2.75 \pm 0.05$ meV) have been derived. The latter corresponds to $K = S^2 D = 6.2 \pm 0.1$ meV ($g = 2.19 \pm 0.09$). Fig. 11b shows the ground state to be $m = \pm 1/2$ since the easy plane anisotropy (equivalent to hard axis) wants to minimize the projection of S onto the designated axis. The field splitting is larger for $m = \pm 3/2$ than for $m = \pm 1/2$ and therefore the $m = 1/2 \rightarrow 3/2$ spin excitation shifts down in energy.

In addition to the two conductance steps, the zero-field spectrum shows a prominent resonance at E_F . This resonance has a Fano lineshape with a very small interference term, making it appear almost Lorentzian. Its temperature dependence is the expected one for a Kondo resonance, and the asymptotic zero Kelvin width determines the Kondo temperature, $T_K = \text{FWHM}(0 \text{ K})/2 k_B = 2.6 \pm 0.2$ K [158]. Such Kondo resonances have been observed with STM for surface adsorbed atoms [17,18] and molecules [159,160].

Co on $\text{Cu}_2\text{N}/\text{Cu}(100)-(2 \times 2)$ displays the Kondo effect, while Fe and Mn on the same substrate do not (see Fe spectra in Section

3.3 and Mn spectra in Ref. [135]). All three adatoms are high-spin impurities as they have $S > 1/2$. They distinguish themselves by the magneto-crystalline anisotropy. Co has a hard axis anisotropy ($D > 0$) while Fe and Mn both have easy axis anisotropy ($D < 0$). Both types of anisotropy create a twofold degenerate zero field ground state. However, for easy axis this state is a doublet with $|m| > 1/2$ which is linked by $\Delta m > 1$ excluding magnetic interactions with single host electrons and thus disabling first order Kondo scattering. Only for high-spin impurities with hard axis is there an $|m| = 1/2$ doublet ground state enabling Kondo screening via $\Delta m = 1$ single electron spin flips.

From the level scheme in Fig. 11b it is clear that low-energy $m = 1/2 \rightarrow -1/2$ spin excitations are expected as the magnetic field splits the two states in energy. These transitions are indeed found in the spectra in Fig. 11a. The conductance steps are superimposed onto the Kondo resonance, which splits in the magnetic field in the very same way as the energy of the lowest lying spin excitation. The pure Kondo features of the LDOS can be retrieved by subtracting the calculated conductance resulting from inelastic spin excita-

tions (yellow curves) from the spectra, leading to Zeemann split Kondo resonances on an almost flat background [158]. Similar field-induced splitting of the Kondo resonance has been observed in electron droplets created by gate electrodes in 2DEGs [161], in lithographically defined Coulomb blockaded quantum dots (QDs) with odd number of electrons on them [162], and for surface impurities [20].

Crystal field effects are entirely absent for Ti on the same substrate, as shown in Fig. 11c. There are no conductance steps due to spin excitations but a clear Kondo peak. Its splitting is identical for all field directions. This is in agreement with Ti having $S = 1/2$. According to Eq. (3) such an impurity can have no anisotropy since the magnitude of m cannot change.

The results discussed in this section show that high-spin impurities exposed to crystal fields giving rise to $D > 0$ display the Kondo effect, while those with $D < 0$ do not. For molecular magnets it has been suggested that mixing of states by large E -values can lead to ground state doublets linked by $\Delta m = 1$ even in the case of $D < 0$ [163]. One could therefore define a more general necessary condition for the anisotropy giving rise to the Kondo effect of high-spin impurities, *i.e.*, the magnetic anisotropy has to create a twofold degenerate ground state linked by $\Delta m = 1$. Whether this is also a sufficient condition has yet to be explored. Similar action of the magnetic anisotropy as the one described above has been proposed for high-spin impurities in bulk [164,165] showing the relevance of the present results derived from surface science for bulk impurities, but also for molecular magnets.

4. Conclusions and future directions

It is now possible with XMCD to determine K , m_S , m_L , and Δm_L of isolated adatoms down to coverages of 0.002 ML. This has been done for magnetic atoms on alkali and transition-metal, as well as semiconductor surfaces. Experiments with magnetic atoms bound to organic molecules [166] or on monolayer thick insulators are on their way. With STM, a smooth and fully reversible transition from tunneling to contact on single adatoms has become possible, enabling controlled quantized conductance measurements, in particular investigation of the possible blocking of one spin conduction channel. Entire magnetization curves for single atoms have been reported with SP-STM. They have to be corrected for the stray field and magnetization reversal of the foremost tip atoms, and could already be used to map RKKY interaction energies through switching field variations as function of distance from a monolayer high ferromagnetic stripe. Effective spin moments and the anisotropy values D and E could be inferred from spin excitation spectra. The intensities of these inelastic transitions are high for adatoms on thin insulating layers, however, detection of such transitions in metal/metal systems may as well become feasible [167]. This would establish direct comparison with the XMCD measurements. The improved experimental access to the magnetism of adatoms on single crystal surfaces described in this paper not only increases our fundamental understanding of low-dimensional magnetism, but has impact on the Physics of magnetic impurities in solids. For instance, the necessary conditions for the Kondo effect of high spin impurities have been identified, and solutions to open issues in dilute magnetic semiconductors could be provided.

Future research will address the necessary conditions for remanence in small magnetic structures, such as single atoms or islands composed of a few atoms only. The studies described above have revealed the magnetic ground state of single atoms to be a superposition of several quantum numbers m . The atom can be prepared by high fields in a state maximizing the amplitude for a single m value. However, what happens when the field is turned off? How fast does it relax, does this depend on the existence of transverse

E -terms in the anisotropy landscape seen by the moment, is this relaxation slow or even absent if there is only a large D -term, and if there is remanence, where is the magnetic energy dissipated? We note that the paramagnetic $M(H)$ -curves for Co/Pt(111) have been measured with SP-STs at electron energies far beyond the threshold for spin excitations of that system opening up the question whether such curves recorded at $V_1 < 9$ meV would display hysteresis. Very interesting future research directions are opening up when the techniques described above begin to be applied to molecular magnets, to metal-organic networks containing magnetic metal centers, or to magnetic impurities on graphene and other thin films with interesting electronic properties.

Acknowledgements

We acknowledge the ESRF for provision of beamtime and financial support by the EUROCORES 05-SONS-FP-009 SANMAG project of the European Science Foundation. PG acknowledges financial support through the SYNSPIN MAT2007-62341 project of the Spanish Ministerio de Educación y Ciencia. We thank H.C. Siegmann and W. Wulfhekel for fruitful discussions, R. Gusmeroli and C. Dallera for providing open access to the Multiplet Inner-Shell Spectroscopy INTERactive GUI of Cowan, Butler, and Thole's multiplet calculation code, L. Bürgi, D.M. Eigler, C.P. Lutz, A. Otte, A. Heinrich, and R. Wiesendanger for allowing us to reproduce figures from their work, and finally C.-L. Bandelier for preparation of the figures.

References

- [1] G. Grosso, G.P. Parravicini, Solid State Physics, Academic Press, London, 2000.
- [2] J.S. Griffith, The Theory of Transition-Metal Ions, Cambridge University Press, Cambridge, 1961.
- [3] H. Brune, Surf. Sci. Rep. 31 (1998) 121.
- [4] D. Gatteschi, R. Sessoli, J. Villain, Molecular Nanomagnets, Oxford University Press, Oxford, 2006.
- [5] M.N. Leuenberger, D. Loss, Nature 410 (2001) 789.
- [6] F. Meier, J. Levy, D. Loss, Phys. Rev. Lett. 90 (2003) 047901.
- [7] G. Bergmann, Phys. Today 32 (1979) 25.
- [8] G. Bergmann, J. Magn. Mater. 35 (1983) 68.
- [9] J.S. Moodera, R. Meserve, Phys. Rev. B 34 (1986) 379.
- [10] P. Gambardella, S.S. Dhesi, S. Gardonio, C. Grazioli, P. Ohresser, C. Carbone, Phys. Rev. Lett. 88 (2002) 047202.
- [11] P. Gambardella, S. Rusponi, M. Veronese, S.S. Dhesi, C. Grazioli, A. Dallmeyer, I. Cabria, R. Zeller, P.H. Dederichs, K. Kern, C. Carbone, H. Brune, Science 300 (2003) 1130.
- [12] P. Gambardella, A. Dallmeyer, K. Maiti, M.C. Malagoli, S. Rusponi, P. Ohresser, W. Eberhardt, C. Carbone, K. Kern, Phys. Rev. Lett. 93 (2004) 077203.
- [13] P. Gambardella, H. Brune, S.S. Dhesi, P. Bencok, S.R. Krishnakumar, S. Gardonio, M. Veronese, C. Grazioli, C. Carbone, Phys. Rev. B 72 (2005) 045337.
- [14] P. Ohresser, H. Boulou, S.S. Dhesi, C. Boeglin, B. Lazarovits, E. Gaudry, I. Chado, J. Faerber, F. Scheurer, Phys. Rev. Lett. 95 (2005) 195901.
- [15] J. Honolka, K. Kuhnke, L. Vitali, A. Enders, S. Gardonio, C. Carbone, K. Kern, P. Bencok, S. Stepanow, P. Gambardella, Phys. Rev. B 76 (2007) 144412.
- [16] A. Yazdani, B.A. Jones, C.P. Lutz, M.F. Crommie, D.M. Eigler, Science 275 (1997) 1767.
- [17] J. Li, W.D. Schneider, R. Berndt, B. Delley, Phys. Rev. Lett. 80 (1998) 2893.
- [18] V. Madhavan, W. Chen, T. Jamneala, M.F. Crommie, N.S. Wingreen, Science 280 (1998) 567.
- [19] P. Wahl, L. Diekhöner, M.A. Schneider, L. Vitali, G. Wittich, K. Kern, Phys. Rev. Lett. 93 (2004) 176603.
- [20] A.J. Heinrich, J.A. Gupta, C.P. Lutz, D.M. Eigler, Science 306 (2004) 466.
- [21] C.F. Hirjibehedin, C.Y. Lin, A.F. Otte, M. Ternes, C.P. Lutz, B.A. Jones, A.J. Heinrich, Science 317 (2007) 1199.
- [22] Y. Yayon, V.W. Brar, L. Senapati, S.C. Erwin, M.F. Crommie, Phys. Rev. Lett. 99 (2007) 067202.
- [23] F. Meier, L. Zhou, J. Wiebe, R. Wiesendanger, Science 320 (2008) 82.
- [24] J. Stöhr, H.C. Siegmann, Magnetism – from Fundamentals to Nanoscale Dynamics, vol. 152, Springer, Berlin, 2006.
- [25] B.T. Thole, P. Carra, F. Sette, G.v.d. Laan, Phys. Rev. Lett. 68 (1992) 1943.
- [26] P. Carra, B.T. Thole, M. Altarelli, X. Wang, Phys. Rev. Lett. 70 (1993) 694.
- [27] C.T. Chen, Y.U. Idzderda, H.J. Lin, N.V. Smith, G. Meigs, E. Chaban, G.H. Ho, E. Pellegrin, F. Sette, Phys. Rev. Lett. 75 (1995) 152.
- [28] J.P. Franck, F.D. Manchester, D.L. Martin, Proc. Roy. Soc. (London) A 263 (1961) 494.
- [29] J. Friedel, Nuovo Cimento Suppl. 7 (1958) 287.
- [30] P.W. Anderson, Phys. Rev. 124 (1961) 41.

- [31] D. Riegel, H.J. Barth, L. Büermann, H. Haas, C. Stenzel, *Phys. Rev. Lett.* 57 (1986) 388.
- [32] R. Kowalik, H.H. Bertsch, K. Biedermann, H. Haas, W. Müller, B. Spellmeyer, W.D. Zeitz, *Phys. Rev. Lett.* 63 (1989) 434.
- [33] H. Beckmann, G. Bergmann, *Phys. Rev. Lett.* 83 (1999) 2417.
- [34] M. Gruyters, D. Riegel, *Phys. Rev. Lett.* 85 (2000) 1582.
- [35] P. Mohn, P. Weinberger, B. Ujfalussy, O. Eriksson, G. Gutierrez, R. Ahuja, B. Johansson, *Phys. Rev. Lett.* 85 (2000) 1583.
- [36] H. Beckmann, G. Bergmann, *Phys. Rev. Lett.* 85 (2000) 1584.
- [37] G. Bergmann, M. Hossain, *Phys. Rev. Lett.* 86 (2001) 2138.
- [38] F. Song, G. Bergmann, *Phys. Rev. Lett.* 88 (2002) 167202.
- [39] S.K. Kwon, B.I. Min, *Phys. Rev. Lett.* 84 (2000) 3970.
- [40] G.Y. Guo, *Phys. Rev. B* 62 (2000) 14609.
- [41] G.v.d. Laan, B.T. Thole, *Phys. Rev. B* 43 (1991) 13401.
- [42] P. Gambardella, A. Dallmeyer, K. Maiti, M.C. Malagoli, W. Eberhardt, K. Kern, C. Carbone, *Nature* 416 (2002) 301.
- [43] L.L. Hirst, *Phys. Kondens. Materie* 11 (1970) 255.
- [44] M. Tischer, O. Hjortstam, D. Arvanitis, J.H. Dunn, F. May, K. Baberschke, J. Trygg, J.M. Wills, B. Johansson, O. Eriksson, *Phys. Rev. Lett.* 75 (1995) 1602.
- [45] D. Weller, J. Stöhr, R. Nakajima, A. Carl, M.G. Samant, C. Chappert, R. Mégy, P. Beauvillain, P. Veillet, G.A. Held, *Phys. Rev. Lett.* 75 (1995) 3752.
- [46] H.A. Dürr, S.S. Dhesi, E. Dudzik, D. Knabben, G.v.d. Laan, J.B. Goedkoop, F.U. Hillebrecht, *Phys. Rev. B* 59 (1999) R701.
- [47] T. Koide, H. Miyauchi, J. Okamoto, T. Shidara, A. Fujimori, H. Fukutani, K. Amemiya, H. Takeshita, S. Yuasa, T. Katayama, Y. Suzuki, *Phys. Rev. Lett.* 87 (2001) 257201.
- [48] V.S. Stepanyuk, W. Hergert, K. Wildberger, R. Zeller, P.H. Dederichs, *Phys. Rev. B* 53 (1996) 2121.
- [49] B. Lazarovits, L. Szunyogh, P. Weinberger, *Phys. Rev. B* 67 (2003) 024415.
- [50] O. Siper, S. Bornemann, J. Minár, S. Polesya, V. Popescu, A. Simunek, H. Ebert, J. Phys. Condens. Matter 19 (2007) 096203.
- [51] G.J. Nieuwenhuys, *Adv. Phys.* 24 (1975) 515.
- [52] D. Weller, A. Moser, *IEEE Trans. Magn.* 35 (1999) 4423.
- [53] N. Nakajima, T. Koide, T. Shidara, H. Miyauchi, H. Fukutani, A. Fujimori, K. Iio, T. Katayama, M. Nyvlt, Y. Suzuki, *Phys. Rev. Lett.* 81 (1998) 5229.
- [54] P. Bruno, *Phys. Rev. B* 39 (1989) 865.
- [55] G.v.d. Laan, J. Phys.-Condens. Matter 10 (1998) 3239.
- [56] I.V. Solovvey, P.H. Dederichs, I. Mertig, *Phys. Rev. B* 52 (1995) 13419.
- [57] S. Chikazumi, *Physics of Ferromagnetism*, Clarendon Press, Oxford, 1997.
- [58] I.M.L. Billas, A. Châtelain, W.A. d. Heer, *Science* 265 (1994) 1682.
- [59] K.W. Edmonds, C. Binns, S.H. Baker, S.C. Thornton, C. Norris, J.B. Goedkoop, M. Finazzi, N.B. Brookes, *Phys. Rev. B* 60 (1999) 472.
- [60] J.T. Lau, A. Föhlisch, R. Nietubyc, M. Reif, W. Wurth, *Phys. Rev. Lett.* 89 (2002) 057201.
- [61] J. Bansmann, S.H. Baker, C. Binns, J.A. Blackman, J.P. Bucher, J. Dorantes-Dávila, V. Dupuis, L. Favre, D. Kechrakos, A. Kleibert, K.H. Meiwes-Broer, G.M. Pastor, A. Perez, O. Toulemonde, K.N. Trohidou, J. Tuailon, Y. Xie, *Surf. Sci. Rep.* 56 (2005) 189.
- [62] R. Wu, C. Li, A.J. Freeman, *J. Magn. Magn. Mater.* 99 (1991) 71.
- [63] S. Rusponi, T. Cren, N. Weiss, M. Epple, P. Bulushek, L. Claude, H. Brune, *Nat. Mater.* 2 (2003) 546.
- [64] P. Gambardella, J. Phys.: Condens. Matter 15 (2003) S2533.
- [65] A. Dallmeyer, C. Carbone, W. Eberhardt, C. Pampuch, O. Rader, W. Gudat, P. Gambardella, K. Kern, *Phys. Rev. B* 61 (2000) R5133.
- [66] H. Ohno, A. Shen, F. Matsukura, A. Oiwa, A. Endo, S. Katsumoto, Y. Iye, *Appl. Phys. Lett.* 69 (1996) 363.
- [67] Y.D. Park, A.T. Hanbicki, S.C. Erwin, C.S. Hellberg, J.M. Sullivan, J.E. Mattson, T.F. Ambrose, A. Wilson, G. Spanos, B.T. Jonker, *Science* 295 (2002) 651.
- [68] H. Shimizu, T. Hayashi, T. Nishinaga, M. Tanaka, *Appl. Phys. Lett.* 74 (1999) 398.
- [69] T. Hayashi, Y. Hashimoto, S. Katsumoto, Y. Iye, *Appl. Phys. Lett.* 78 (2001) 1691.
- [70] K.W. Edmonds, P. Boguslawski, K.Y. Wang, R.P. Campion, S.N. Novikov, N.R.S. Farley, B.L. Gallagher, C.T. Foxon, M. Sawicki, T. Dietl, M.B. Nardelli, J. Bernholc, *Phys. Rev. Lett.* 92 (2004) 037201.
- [71] P. Gambardella, L. Claude, S. Rusponi, K.J. Franke, H. Brune, J. Raabe, F. Nolting, P. Bencok, A.T. Hanbicki, B.T. Jonker, C. Grazioli, M. Veronese, C. Carbone, *Phys. Rev. B* 75 (2007) 125211.
- [72] S.J. Potashnik, K.C. Ku, R. Mahendiran, S.H. Chun, R.F. Wang, N. Samarth, P. Schiffer, *Phys. Rev. B* 66 (2002) 012408.
- [73] H. Ohldag, V. Solinus, F.U. Hillebrecht, J.B. Goedkoop, M. Finazzi, F. Matsukura, H. Ohno, *Appl. Phys. Lett.* 76 (2000) 2928.
- [74] S. Ueda, S. Imada, T. Muro, Y. Saitoh, S. Suga, F. Matsukura, H. Ohno, *Physica E* 10 (2001) 210.
- [75] Y.L. Soo, G. Kioseoglou, S. Kim, X. Chen, H. Luo, Y.H. Kao, H.J. Lin, H.H. Hsieh, T.Y. Hou, C.T. Chen, Y. Sasaki, X. Liu, J.K. Furdyna, *Phys. Rev. B* 67 (2003) 214401.
- [76] K.W. Edmonds, N.R.S. Farley, R.P. Campion, C.T. Foxon, B.L. Gallagher, T.K. Johal, G.v.d. Laan, M. MacKenzie, J.N. Chapman, E. Arenholz, *Appl. Phys. Lett.* 84 (2004) 4065.
- [77] Y.J. Zhao, W.T. Geng, K.T. Park, A.J. Freeman, *Phys. Rev. B* 64 (2001) 035207.
- [78] P. Mahadevan, A. Zunger, *Phys. Rev. B* 69 (2004) 115211.
- [79] Y.J. Zhao, T. Shishidou, A.J. Freeman, *Phys. Rev. Lett.* 90 (2003) 047204.
- [80] A. Stroppa, S. Picozzi, A. Continenza, A.J. Freeman, *Phys. Rev. B* 68 (2003) 155203.
- [81] H.A. Dürr, G.v.d. Laan, D. Spanke, F.U. Hillebrecht, N.B. Brookes, *Phys. Rev. B* 56 (1997) 8156.
- [82] K.W. Edmonds, N.R.S. Farley, T.K. Johal, G.v.d. Laan, R.P. Campion, B.L. Gallagher, C.T. Foxon, *Phys. Rev. B* 71 (2005) 064418.
- [83] D.J. Keavney, D. Wu, J.W. Freeland, E. Johnston-Halperin, D.D. Awschalom, J. Shi, *Phys. Rev. Lett.* 91 (2003) 187203.
- [84] G. Profeta, S. Picozzi, A. Continenza, C. Franchini, *Phys. Rev. B* 70 (2004) 155307.
- [85] W. Zhu, H.H. Weitering, E.G. Wang, E. Kaxiras, Z. Zhang, *Phys. Rev. Lett.* 93 (2004) 126102.
- [86] A.M. Nazmul, S. Sugahara, M. Tanaka, *Appl. Phys. Lett.* 80 (2002) 3120.
- [87] W.D. Schneider, R. Berndt, J. El. Spectr. Rel. Phen. 109 (2000) 19.
- [88] M.F. Crommie, J. El. Spectr. Rel. Phen. 109 (2000) 1.
- [89] M. Ternes, A.J. Heinrich, W.D. Schneider, *J. Phys.: Condens. Matter* 21 (2009) 053001.
- [90] F. Patthey, J.M. Imer, W.D. Schneider, H. Beck, Y. Baer, B. Delley, *Phys. Rev. B* 42 (1990) 8864.
- [91] D. Malterre, M. Grioni, Y. Baer, *Adv. Phys.* 45 (1996) 299.
- [92] M. Garnier, K. Breuer, D. Purdie, M. Hengsberger, Y. Baer, B. Delley, *Phys. Rev. Lett.* 78 (1997) 4127.
- [93] L.E. Davis, M.P. Everson, R.C. Jaklevic, W. Shen, *Phys. Rev. B* 43 (1991) 3821.
- [94] M.F. Crommie, C.P. Lutz, D.M. Eigler, *Nature* 363 (1993) 524.
- [95] P. Avouris, I.W. Lyo, R.E. Walkup, Y. Hasegawa, *J. Vac. Sci. Technol. B* 12 (1994) 1447.
- [96] S.K. Upadhyay, A. Palanisami, R.N. Louie, R.A. Buhrman, *Phys. Rev. Lett.* 81 (1998) 3247.
- [97] R.J. Soulen, J.M. Byers, M.S. Osofsky, B. Nadgorny, T. Ambrose, C.F. Cheng, P.R. Broussard, C.T. Tanaka, J. Nowak, J.S. Moodera, A. Barry, J.M.D. Coey, *Science* 282 (1998) 85.
- [98] N. Agrait, J.G. Rodrigo, S. Vieira, *Phys. Rev. B* 46 (1992) 5814.
- [99] O. Naaman, R.C. Dynes, *Sol. State Commun.* 129 (2004) 299.
- [100] M. Ternes, W.D. Schneider, J.C. Cuevas, C.P. Lutz, C.F. Hirjibehedin, A.J. Heinrich, *Phys. Rev. B* 74 (2006) 132501.
- [101] L. Bürgi, Ph.D. Thesis. Swiss Federal Institute of Technology, Lausanne, 1999.
- [102] M.Y. Zhuravlev, E.Y. Tsymlal, S.S. Jaswal, A.V. Vedyayev, B. Dieny, *Appl. Phys. Lett.* 83 (2003) 3534.
- [103] R. Landauer, *Z. Phys. B: Cond. Matter* 68 (1987) 217.
- [104] B.J.v. Wees, H.v. Houten, C.W.J. Beenakker, J.G. Williamson, L.P. Kouwenhoven, D.v.d. Marel, C.T. Foxon, *Phys. Rev. Lett.* 60 (1988) 848.
- [105] D.A. Wharam, T.J. Thornton, R. Newbury, M. Pepper, H. Ahmed, J.E.F. Frost, D.G. Hasko, D.C. Peacock, D.A. Ritchie, G.A.C. Jones, *J. Phys. C* 21 (1988) L209.
- [106] C.J. Muller, J.M.V. Ruitenbeek, L.J. d. Jong, *Phys. Rev. Lett.* 69 (1992) 140.
- [107] J.M. Krans, J.M.V. Ruitenbeek, V.V. Fisun, I.K. Yanson, L.J. d. Jongh, *Nature* 375 (1995) 767.
- [108] W.A.d. Heer, S. Frank, D. Ugarte, Z. Phys. B: Cond. Matter 104 (1997) 469.
- [109] E. Scheer, N. Agrait, J.C. Cuevas, A.L. Yeyati, B. Ludoph, A.M. Rodero, G.R. Bollinger, J.M.V. Ruitenbeek, C. Urbina, *Nature* 394 (1998) 154.
- [110] J.L. Costa-Krämer, N. Garcia, P. Garcia-Mochales, P.A. Serena, *Surf. Sci.* 342 (1995) L1144.
- [111] N. Agrait, G. Rubio, S. Vieira, *Phys. Rev. Lett.* 74 (1995) 3995.
- [112] G. Rubio, N. Agrait, S. Vieira, *Phys. Rev. Lett.* 76 (1996) 2302.
- [113] L. Olesen, E. Lægsgaard, I. Stensgaard, F. Besenbacher, J. Schiøtz, P. Stoltze, K.W. Jacobsen, J.K. Nørskov, *Phys. Rev. Lett.* 72 (1994) 2251.
- [114] A. Yazdani, D.M. Eigler, N.D. Lang, *Science* 272 (1996) 1921.
- [115] L. Limot, J. Kröger, R. Berndt, A. Garcia-Lekue, W.A. Hofer, *Phys. Rev. Lett.* 94 (2005) 126102.
- [116] J. Kröger, H. Jensen, R. Berndt, N. J. Phys. 9 (2007) 153.
- [117] J.K. Gimzewski, R. Möller, *Phys. Rev. B* 36 (1987) 1284.
- [118] J.M. Krans, C.J. Muller, I.K. Yanson, T.C.M. Govaert, R. Hesper, J.M.V. Ruitenbeek, *Phys. Rev. B* 48 (1993) 14721.
- [119] J. Kröger, N. Néel, L. Limot, *J. Phys. Cond. Mat.* 20 (2008) 223001.
- [120] L. Vitali, R. Ohmann, S. Stepanow, P. Gambardella, K. Tao, R. Huang, V.S. Stepanyuk, P. Bruno, K. Kern, *Phys. Rev. Lett.* 101 (2008) 216802.
- [121] A.A. Abrikosov, L.P. Gor'kov, *Zh. Eksp. Teor. Fiz.* 39 (1962) 1781.
- [122] M.A. Woolf, F. Reif, *Phys. Rev.* 137 (1965) A557.
- [123] W. Bauriedl, P. Ziemann, W. Buckel, *Phys. Rev. Lett.* 47 (1981) 1163.
- [124] E.W. Hudson, K.M. Lang, V. Madhavan, S.H. Pan, H. Eisaki, S. Uchida, J.C. Davis, *Nature* 411 (2001) 920.
- [125] M. Ternes, Ph.D. Thesis. Swiss Federal Institute of Technology, Lausanne, 2006.
- [126] O. Naaman, W. Teizer, R.C. Dynes, *Rev. Sci. Instrum.* 72 (2001) 1688.
- [127] S.H. Pan, E.W. Hudson, J.C. Davis, *Appl. Phys. Lett.* 73 (1998) 2992.
- [128] J.G. Rodrigo, H. Suderow, S. Vieira, *Europ. Phys. J. B* 40 (2004) 483.
- [129] H. Suderow, E. Bascones, A. Izquierdo, F. Guinea, S. Vieira, *Phys. Rev. B* 65 (2002) 100519.
- [130] R. Meservey, *Phys. Scr.* 38 (1988) 272.
- [131] R. Meservey, P.M. Tedrow, *Phys. Rep.* 238 (1994) 173.
- [132] T. Soda, T. Matsuura, Y. Nagaoka, *Prog. Theor. Phys.* 38 (1967) 551.
- [133] H. Shiba, *Prog. Theor. Phys.* 40 (1968) 435.
- [134] A. Sakurai, *Prog. Theor. Phys.* 44 (1970) 1472.
- [135] C.F. Hirjibehedin, C.P. Lutz, A.J. Heinrich, *Science* 312 (2006) 1021.
- [136] J. Lambe, R.C. Jaklevic, *Phys. Rev.* 165 (1968) 821.
- [137] E.L. Wolf, *Principles of Electron Tunneling Spectroscopy*, Oxford University Press, New York, 1989.
- [138] B.C. Stipe, M.A. Rezaei, W. Ho, *Science* 280 (1998) 1732.

- [139] T. Balashov, A.F. Takacs, W. Wulfhekel, J. Kirschner, *Phys. Rev. Lett.* 97 (2006) 187201.
- [140] G. Kresse, M. Schmid, E. Napetschnig, M. Shishkin, L. Köhler, P. Varga, *Science* 308 (2005) 1440.
- [141] H. Ellmer, V. Repain, M. Sotto, S. Rousset, *Surf. Sci.* 511 (2002) 183.
- [142] B. Croset, Y. Girard, G. Prtvoť, M. Sotto, Y. Garreau, R. Pinchaux, M. Sauvage-Simkin, *Phys. Rev. Lett.* 88 (2002) 56103.
- [143] D.M. Eigler, C.P. Lutz, W.E. Rudge, *Nature* 352 (1991) 600.
- [144] L. Bartels, G. Meyer, K.H. Rieder, *Phys. Rev. Lett.* 79 (1997) 697.
- [145] H. Brune, *Science* 312 (2006) 1005.
- [146] R. Wiesendanger, H.J. Güntherodt, G. Güntherodt, R.J. Gambino, R. Ruf, *Phys. Rev. Lett.* 65 (1990) 247.
- [147] M. Bode, *Rep. Prog. Phys.* 66 (2003) 523.
- [148] W. Wulfhekel, J. Kirschner, *Ann. Rev. Mater. Res.* 37 (2007) 69.
- [149] M. Bode, M. Heide, K.V. Bergmann, P. Ferriani, S. Heinze, G. Bihlmayer, A. Kubetzka, O. Pietzsch, S. Blügel, R. Wiesendanger, *Nature* 447 (2007) 190.
- [150] S. Rusponi, N. Weiss, T. Cren, M. Epple, H. Brune, *Appl. Phys. Lett.* 87 (2005) 162514.
- [151] W.A. Hofer, K. Palotás, S. Rusponi, T. Cren, H. Brune, *Phys. Rev. Lett.* 100 (2008) 026806.
- [152] S. Krause, L. Berbil-Bautista, G. Herzog, M. Bode, R. Wiesendanger, *Science* 317 (2007) 1537.
- [153] Y. Yayon, X.H. Lu, M.F. Crommie, *Phys. Rev. B* 73 (2006) 155401.
- [154] M.A. Ruderman, C. Kittel, *Phys. Rev.* 96 (1954) 99.
- [155] T. Kasuya, *Prog. Theor. Phys.* 16 (1956) 45.
- [156] K. Yosida, *Phys. Rev.* 106 (1957) 893.
- [157] J. Wiebe, F. Meier, K. Hashimoto, G. Bihlmayer, S. Blügel, P. Ferriani, S. Heinze, R. Wiesendanger, *Phys. Rev. B* 72 (2005) 193406.
- [158] A.F. Otte, M. Ternes, K.V. Bergmann, S. Loth, H. Brune, C.P. Lutz, C.F. Hirjibehedin, A.J. Heinrich, *Nature Phys.* 8 (2008) 847.
- [159] A. Zhao, Q. Li, L. Chen, H. Xiang, W. Wang, S. Pan, B. Wang, X. Xiao, J. Yang, J.G. Hou, Q. Zhu, *Science* 309 (2005) 1542.
- [160] P. Wahl, L. Diekhöner, G. Wittich, L. Vitali, M.A. Schneider, K. Kern, *Phys. Rev. Lett.* 95 (2005) 166601.
- [161] D. Goldhaber-Gordon, H. Shtrikman, D. Mahalu, D. Abusch-Magder, U. Meirav, M.A. Kastner, *Nature* 391 (1998) 156.
- [162] S.M. Cronenwett, T.H. Oosterkamp, L.P. Kouwenhoven, *Science* 281 (1998) 540.
- [163] C. Romeike, M.R. Wegewijs, W. Hofstetter, H. Schöller, *Phys. Rev. Lett.* 96 (2006) 196601.
- [164] P. Schlottmann, *Phys. Rev. B* 30 (1984) 1454.
- [165] B. Ujjfalussy, L. Szunyogh, P. Bruno, P. Weinberger, *Phys. Rev. Lett.* 77 (1996) 1805.
- [166] P. Gambardella, S. Stepanow, A. Dmitriev, J. Honolka, F.M.F. de Groot, M. Lingenfelder, S.S. Gupta, D.D. Sarma, P. Bencok, S. Stanescu, S. Clair, S. Pons, N. Lin, A.P. Seitsonen, H. Brune, J.V. Barth, K. Kern, *Nat. Mater.* 8 (2009) 189.
- [167] W. Wulfhekel, private communication.
- [168] A.F. Otte, *Europhys. News* 39 (2008) 31.